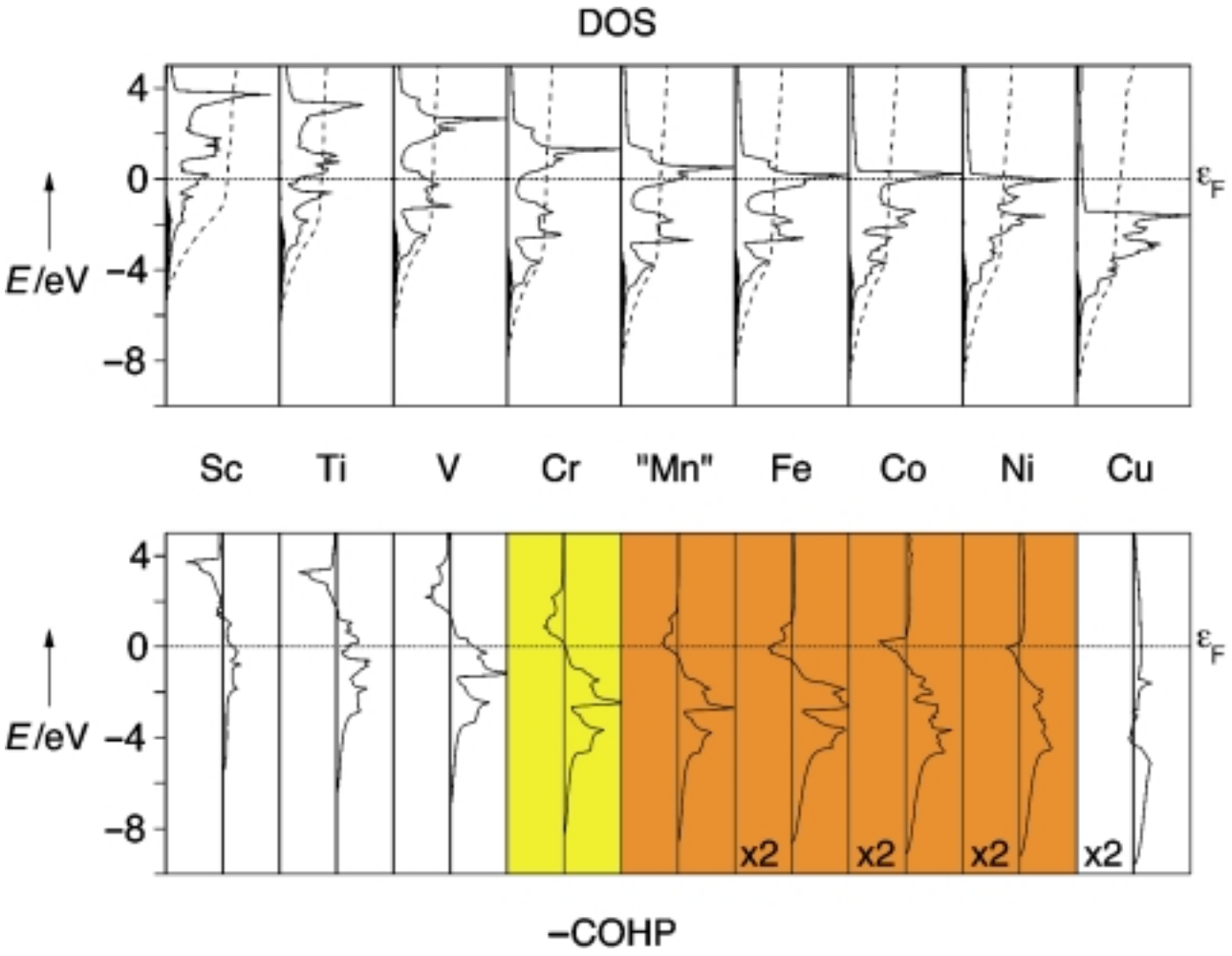

ANGEWANDTE CHEMIE ©WILEY-VCH

The picture shows the non-spin-polarized density of states (DOS; above) and M-M crystal-orbital Hamilton population (COHP; below) curves for the first transition metal series. For the early transition metals like Ti, the Fermi level ε_F lies low in the COHP curve and thereby falls in the M-M bonding region. As a result, there exists no drive towards ferromagnetism for the early transition metals. For Cr, ε_F lies in the COHP curve between the bonding and antibonding regions, whereas for the metals from "Mn" (the body-centered cubic form of Mn) to Ni, ε_F lies in the region that is clearly responsible for M-M antibonding: Fe, Co, and Ni are all ferromagnetic.

The Orbital Origins of Magnetism: From Atoms to Molecules to Ferromagnetic Alloys

Gregory A. Landrum and Richard Dronskowski*

Dedicated to Professor Arndt Simon on the occasion of his 60th birthday

A chemical view of spin magnetic phenomena in finite (atoms and molecules) and infinite (transition metals and their alloys) systems using the concepts of bonding and electronic shielding is presented. The concept is intended to serve as a semiquantitative signpost for the synthesis of new ferromagnets. After a concise overview of the historic development of related theories developed within the physics community, the consequences of spin–spin coupling (made manifest in the exchange or Fermi hole) in atoms and molecules are explored. Upon moving to a paramagnetic state, the majority/minority spin species become more/less tightly bound to the nucleus, resulting in differences in the energies and spatial extents of the two sets of spin orbitals. By extrapolating well-known arguments from ligand-field theory, the paucity of ferromagnetic transition metals arises from quenching the paramagnetism of the free atoms due to strong interatomic interactions in the solid state. Critical valence electron concentrations in Fe, Co, and Ni, however, result in local electronic instabilities due to the population of antibonding states at the Fermi level ε_F. Removal of these antibonding states from the vicinity of ε_F is the origin of ferromagnetism; in the pure metals this results in strengthening the chemical bonds. In the 4d and 5d transition metals, the valence d orbitals are too well shielded from the nucleus, so a transition to a ferromagnetic state does not result in sufficiently large changes to occur. Thus, the exceptional occurence of ferromagnetism only in the first transition series appears to parallel the special main-group chemistry of the first long period. A connection between ferromagnetism in the transition metals and Pearson's absolute hardness η is easily established and shows that ferromagnetism appears only when $\eta < 0.2$ eV in the nonmagnetic calculation. As expected from the principle of maximum hardness, Fe, Co, and Ni all become harder upon moving to the more stable ferromagnetic state. Magnetism in intermetallic alloys follows the same path. Whether or not an alloy contains ferromagnetic elements, the presence of antibonding states at ε_F serves as a "fingerprint" to indicate a ferromagnetic instability. The differences in the sizes of the local magnetic moments on the constituent atoms of a ferromagnetic alloy can be understood in terms of the relative contributions to the density of states at ε_F in the nonmagnetic calculations. Appropriately parameterized, nonmagnetic, semi-empirical calculations can also be used to expose the ferromagnetic instability in elements and alloys. These techniques, which have become relatively commonplace, can be used to guide the synthetic chemist in search of new ferromagnetic materials.

Keywords: alloys · density-functional calculations · electronic structure · magnetic properties · intermetallic phases

1. Introduction

"The magnetic and associated properties of substances which behave magnetically like iron have long provided a happy hunting ground if not for the "smoother pebble than ordinary" at least for the more curiously shaped one. The rich diversity of ferromagnetic phenomena, the perennial challenge to skill in experiment and to physical insight in coordinating the results, the vast range of actual and possible applications of ferromagnetic materials, and the fundamental character of the essential theoretical problems raised have all combined to give ferromagnetism a width of interest which contrasts strongly with the apparent narrowness of its subject matter, namely certain particular properties of a very limited number of substances."[1]

"To understand an observable means being able to predict, albeit qualitatively, the result that a perfectly reliable calculation would yield for that observable."[2]

[*] Prof. Dr. R. Dronskowski, Dr. G. A. Landrum
Institut für Anorganische Chemie
Rheinisch-Westfälische Technische Hochschule
Prof.-Pirlet-Strasse 1, 52056 Aachen (Germany)
Fax: (+49) 241-8888-288
E-mail: drons@HAL9000.ac.rwth-aachen.de

  1433-7851/00/3909-1561 $ 17.50+.50/0

The first of the preceding quotations, describing the state of research into ferromagnetism in 1946, seems almost prescient. Despite active investigation for more than a century, ferromagnetism remains fascinating and somewhat mysterious, at least to most chemists. An incredible amount of effort is still being directed at both characterizing ferromagnetic compounds by experiment and understanding their properties by theory. For example, the condensed-matter physics journal *Physical Review B* in 1998 alone published more than 100 papers devoted to ferromagnetism.[3] Despite its age, the field is still intensely active and contentious, particularly in the physics and materials-science communities. Given the importance of magnetic materials (what would our modern "information society" look like without the potential to magnetically store and retrieve data?), this fascination with magnetism is completely understandable.[4]

Our first aim in this contribution is to briefly summarize the history of attempts to understand ferromagnetism. Although the existence of ferromagnetism can now be numerically reproduced by high-level quantum mechanical computations, many find it surprising that it remains difficult to understand why some materials are ferromagnetic and others are not. We then present a new style of thinking, extracted from the results of first-principles calculations, which explains the occurrence (or absence) of ferromagnetism in the transition metals and their alloys in terms of chemical bonding. We do not presume to promote this model as the quintessential description of ferromagnetism (to do so would be presumptuous). Instead, our hope is that it will provide a clearer understanding, in the spirit of the second quotation, of the phenomenon. More importantly, our intention is to derive a semiquantitative signpost for the skillful experimental chemist to use in the synthesis of new ferromagnetic materials.

2. The Development of a Battlefield: Localized Versus Delocalized Ferromagnetism

To lay the groundwork for what follows, we provide here a concise historical overview of the development of the theory of magnetism and ferromagnetism in particular. This treatment of more than a century's worth of research is, necessarily, incomplete. The interested reader can find a far more complete account of the early history of the science of magnetism in ref. [5].

2.1. Curie and Langevin: Early Experiments and Theories

Drawing upon the results of an extensive series of careful experiments carried out at the end of the 19th century, Pierre Curie divided materials into three distinct types based upon their magnetic behavior: diamagnets (with small, negative, temperature-independent susceptibilities), paramagnets (with small, positive susceptibilities, which typically vary inversely with temperature), and ferromagnets (substances which exhibit magnetism without an applied field below a critical temperature and behave as strong paramagnets at higher temperatures).[6] While Curie's definitions of the types of magnetism are of indisputable importance, they are based upon an empirical approach—observing and describing the observed behavior rather than explaining it.

R. Dronskowski

G. A. Landrum

Richard Dronskowski was born in Brilon (Germany) in 1961. He studied chemistry and physics from 1981 until 1989 and received his Diplomas from the University of Münster. In 1990, he completed his doctorate, on the topic of compounds with condensed clusters, at the Max Planck Institute for Solid-State Research (Stuttgart) under the supervision of Prof. Arndt Simon. After a year as a visiting scientist with Roald Hoffmann at Cornell University in 1991 and completing his habilitation in Inorganic Chemistry at Dortmund University in 1995, he accepted in 1996 the offer of the Rheinisch-Westfälische Technische Hochschule in Aachen to become the successor of Welf Bronger. His research interests lie in the region of solid-state chemistry, in particular the synthesis and structural characterization of low-valent as well as magnetic and intermetallic compounds. In the theoretical realm, acid-base properties and the reactivity of solid compounds lie close to his heart, as do questions of chemical bonding and crystal-chemical simulations. The music of Alban Berg and Béla Bartók hold just as much interest for him.

Greg Landrum, born in Baltimore (USA) in 1970, completed his B. S. in chemistry and computer science at Carnegie Mellon University in 1992. In 1997 he received his Ph. D. from Cornell University, where he worked with Roald Hoffmann and studied the electronic structure and bonding of organometallic, intermetallic, and main-group compounds. During his post-doctoral stay at the Rheinisch-Westfälische Technische Hochschule in Aachen he has applied density-functional calculations to the study of nitrides, intermetallic phases, and magnetism. His research interests lie in the use of high-level theoretical methods to construct chemical explanations for the reactivity and properties of molecules and solids. Though his musical tastes are not as refined as those of his co-author, they are just as strongly held.

Paul Langevin, one of Curie's students, introduced in 1905 the idea of the *magnetic moment* in order to explain the experimental data for diamagnetic and paramagnetic materials.[7] Within Langevin's theory, the magnetization M of a paramagnetic substance made up of N molecules or atoms can be expressed by [Eq. (1)], where a is given in [Eq. (2)].

$$\frac{M}{M_0} = \coth a - \frac{1}{a} \tag{1}$$

$$a = \frac{\mu H}{kT} \tag{2}$$

In Equation (2), μ is the magnetic moment of an individual molecule or atom, H is the strength of the applied field, T is the temperature, k is Boltzmann's constant, and $M_0 = N\mu$ is the magnetization of the sample if all magnetic moments are aligned. Langevin explained ferromagnetism by invoking the presence of intermolecular or interatomic interactions which cause individual magnetic moments to align parallel. While the classical theory of paramagnetism was fundamentally flawed—falsely predicting diamagnetic and paramagnetic susceptibilities to be of equal magnitude—it provided a framework for the work of Pierre Weiss.

2.2. Weiss's Molecular Field: a Local View

Only two years later, Weiss developed a radical idea still found in many textbooks. According to Weiss, ferromagnetism depends on the existence of a "molecular field", an enormously large, internal magnetic field in the crystal which acts to align neighboring magnetic moments.[8] This approach adds an extra term h to Equation (2) [Eq. (3)].

$$a = \frac{\mu(H + h)}{kT} \tag{3}$$

This term, where $h = qM$ (q is the molecular field constant), reflects the response of the molecular field to the magnetization of the sample. Weiss demonstrated that the molecular field can give rise to a magnetization in the sample *even when the applied field H is zero*. This "spontaneous magnetization", M_S, can be graphically determined by plotting the Langevin equation [Eq. (1)] using the form of the variable a from [Eq. (3)]. At a given temperature T the spontaneous magnetization is determined by the intersection of the Langevin equation with the line given by [Eq. 4] (Figure 1)

$$M = \left(\frac{k}{q\mu}T\right) a = (cT)a \tag{4}$$

When the temperature T is smaller than the Curie-Weiss temperature T_{CW} (the ferromagnetic ordering temperature; see the dashed line in Figure 1), M_S is determined by the intersection of the curve of the Langevin equation and the line $(cT)a$. When T is larger than T_{CW} (dotted line in Figure 1), there is no such intersection and the spontaneous magnetization is zero.

The physical origin of the molecular field central to Weiss's theory remained mysterious for years. In fact, Weiss himself was never able to provide any meaningful explanation of the huge strength of the molecular field. However, by this hypothesis Weiss showed that the intermolecular or interatomic forces in crystals do not extend beyond a certain "active region." A number of ingenious intermetallic dilution experiments led Weiss to realize that the molecular field in ferromagnetic iron decays with the sixth power of the interatomic distance.[9]

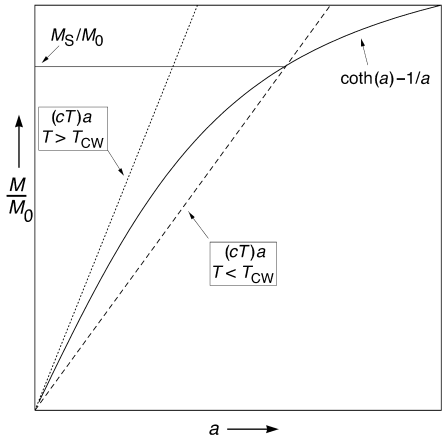

Figure 1. Graphical solution for the spontaneous magnetization M_S of a material within Weiss's theory of ferromagnetism. Refer to the text for details.

2.3. Quantum Mechanics: Heisenberg and Stoner

The puzzle of the molecular field was solved by Heisenberg in 1928[10] and, almost simultaneously, by Dirac.[11] Only four years later, most theoretical expressions had been brought into a self-consistent form by van Vleck in his widely acclaimed textbook on magnetism.[12] The theory shows that ferromagnetism may be understood to arise from quantum-mechanical exchange interactions which lead to the parallel alignment of spins $\vec{S}_i$ and $\vec{S}_j$ [Eq. (5)].

$$V_{ij} = -2J_{ij}\vec{S}_i\vec{S}_j \tag{5}$$

Here, J_{ij}, the exchange integral between atoms i and j, is *positive*. It is important to realize that this view is a *local* one, and it treats the system as if the electrons responsible for ferromagnetism are fixed on the atoms. Thus, Heisenberg's approach bears a strong resemblance to the Heitler–London treatment of the hydrogen molecule. In chemical terminology, the model is similar to valence-bond (VB) theory.

Most chemists will immediately sense the problems inherent in applying Heisenberg's model to the archetypical ferromagnets iron, cobalt, and nickel. In these metals, the experimentally determined magnetic moments (the number of unpaired electrons) are all nonintegral: 2.21, 1.60, and 0.62 for Fe, Co, and Ni, respectively. Clearly, the unpaired spins cannot be fully localized since atom-centered magnetic moments should adopt integer values.[13] It also seems somewhat ill-advised, at best, to assume the presence of localized spins in a metal where the conduction electrons are strongly *delocalized* (itinerant).

The itinerant nature of the conduction electrons in metals had been recognized long prior to Heisenberg's theory of ferromagnetism. An early theory of the electronic structure of metals, developed by Drude and Lorentz, treated the electrons as an ideal gas fully delocalized throughout the crystal. While this theory was quite successful in explaining the conductivity of metals, problems arose with respect to their electronic heat capacities; these were predicted to be much too large. Sommerfeld replaced the classical Boltzmann statistics (appropriate for gas molecules) of the Drude model with Fermi–Dirac statistics (appropriate for electrons), thereby implicitly taking the Pauli exclusion principle into account. The success of Sommerfeld's theory in describing the experimentally observed properties of metals provided solid support for the idea that the conduction electrons are *itinerant*: delocalized throughout the crystal. In what is probably one of the first applications of the rigid-band model to the electronic structure of solids, Slater used the first calculated electronic structure of elemental copper[14] to argue that the ferromagnetism of nickel must be due to these itinerant electrons. Slater went so far as to say that Heisenberg's model of ferromagnetism "is considered to be unsuitable for application to ferromagnetism, except in its general principle of explaining the energy of orientation of elementary magnets in terms of exchange energy."[15]

Based upon this theoretical framework, an alternative treatment of ferromagnetism was proposed by Stoner in 1938–1939.[16, 17] By assuming an average spin field interacting with a single spin (equivalent to a mean-field treatment of electronic correlation) and parabolic energy bands, Stoner presented a predictive model of itinerant-electron ferromagnetism. It is clear that such a delocalized treatment is closely related to the Hund–Mulliken molecular orbital (MO) approach for the hydrogen molecule. Stoner's theory of ferromagnetism is quite detailed. In addition to predicting whether or not a given metal is ferromagnetic, it included methods for calculating the temperature dependence of both the magnetic susceptibility and the electronic specific heat. Here we limit ourselves to discussing the "Stoner criterion" for the presence of ferromagnetism.

The Stoner criterion can be concisely expressed as Equation (6), where I is a measure of the strength of the exchange interaction in the metal and $\mathrm{DOS}(\varepsilon_F)$ is the density of states at the Fermi level, ε_F.

$$I\mathrm{DOS}(\varepsilon_F) > 1 \qquad (6)$$

In the original formulation of the model, I and $\mathrm{DOS}(\varepsilon_F)$ were approximated for the transition metals. Once accurate electronic-structure calculations became possible, $\mathrm{DOS}(\varepsilon_F)$ was also immediately accessible. A number of authors (see, for example, refs. [18, 19], and references therein) proposed various ways to extract I from their results. The first comprehensive tabulation of I and $\mathrm{DOS}(\varepsilon_F)$ pairs was presented by Janak in 1977.[19] His results, along with the product $I\mathrm{DOS}(\varepsilon_F)$, are plotted in Figure 2. Using Janak's parameters, iron and nickel are predicted to be ferromagnetic and palladium is predicted to be almost ferromagnetic; palladium is, in fact, known as an "incipient ferromagnet". The one failure within this model is for cobalt ($I\mathrm{DOS}(\varepsilon_F) = 0.972$), predicted to be nonmagnetic. It is also somewhat strange that nickel, the *weakest* ferromagnet, has the *largest* $I\mathrm{DOS}(\varepsilon_F)$ value.

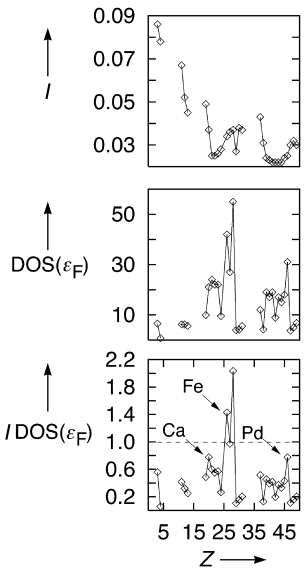

Figure 2. Plots of the Stoner exchange parameter I, $\mathrm{DOS}(\varepsilon_F)$, and $I\mathrm{DOS}(\varepsilon_F)$ versus atomic number Z for selected metallic elements. Metals lying above the dashed line at $I\mathrm{DOS}(\varepsilon_F) = 1$ are predicted to be ferromagnetic. Data are taken from ref. [19].

In the years after their introduction, either the Heisenberg or Stoner approach came into or went out of favor, depending upon the subject and the school of interacting disciplines. This back-and-forth battle is probably all too familiar to many chemists if one recalls the long-time struggle between the VB and MO approaches for the study of bonding in molecules. In 1966, Herring finally demonstrated that the descriptions are not mutually exclusive.[20] In our view, however, the delocalized theory is certainly much better suited to transition metals.

Nowadays, most solid-state physicists accept the Stoner criterion to decide whether or not a metal or alloy should be ferromagnetic. While (with the exception of cobalt) this model is predictive, it doesn't provide much helpful information to use in truly understanding the nature of ferromagnetism; certainly none at all to help in developing a chemical understanding. The original model, derived from an assumed parabolic band shape, does not take into account either the shape of the DOS curves or the position of ε_F within those curves. These are two of the places where the chemistry hides.

3. Magnetism in Atoms and Molecules

The study of spin-spin coupling supplies the key to understanding magnetism, the macroscopic quantum effect. The underlying antisymmetry of the wave functions of a system has a deep impact upon the magnetism and chemistry of atoms and molecules.

3.1. The Exchange Hole and its Consequences

Since the exchange hole, which goes by a number of other names (such as "Fermi hole"), is central to our analysis of ferromagnetism, we briefly discuss it here. Although our discussion relies on results derived for an idealized system (the free-electron gas), we will demonstrate that the general conclusions are applicable to real systems such as atoms, molecules, and crystals.

When two electrons are brought into proximity to each other, they experience a Coulombic repulsion due to their negative charges. Since, by Pauli's principle, two electrons with the same magnetic spin quantum number are forbidden from occupying the same position, there is an extra repulsion between like-spin electrons known as the exchange repulsion. One of the major consequences of this repulsion is the appearance of the exchange hole in the free-electron gas. For a given α (spin-up) electron, it experiences an effective electron density arising from all of the other electrons in the electron gas. The effective density close to the electron is relatively low because the Coulomb repulsion keeps all of the other electrons away. The exchange repulsion results in a further depletion of the α-electron density, but does not affect the β spins. This "hole" in the effective α-electron density (α-α curve in Figure 3) is known as the exchange hole. No such hole exists in the α-β curve.

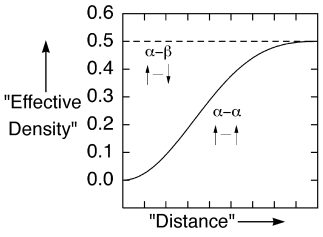

Figure 3. A schematic illustration of the exchange hole.

Although the perturbations to the electron density arising from the exchange term are quite small compared to those from the Coulombic interactions, their effects can be extraordinarily important. Because of the exchange hole, like-spin electrons do not shield each other from the nucleus as well as electrons with different spins, that is, α-α shielding is less effective than α-β shielding. Thus there is a differential shielding of α and β electrons in systems with unpaired spins. If we assume, for simplicity, that the α electrons are the majority spin species, then they will be, on average, less shielded from the nucleus than the β electrons. Consequently the α electrons experience a higher effective nuclear charge than the β electrons. The differences in effective nuclear charge for the two spin species lead immediately to energy differences in the orbitals associated with each spin.

3.2. Light Atoms

Figure 4 shows the changes in energy levels of atomic oxygen upon moving from a singlet to a triplet state. When the spins are allowed to unpair (a process we will refer to as spin-polarization), the α electrons, which are now less shielded due to the smaller number of β electrons, drop in energy. At the same time, the β spins experience greater shielding and the associated spin orbitals increase in energy. The resulting splittings between equivalent α and β spin orbitals (the exchange splittings) in triplet atomic oxygen are

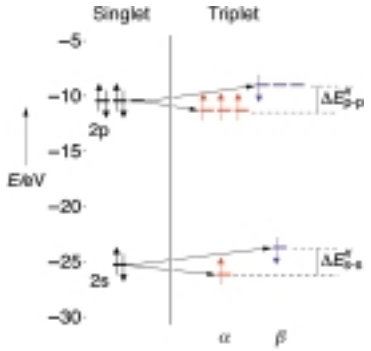

Figure 4. Energy level diagrams for atomic oxygen in a singlet excited state (left) and the triplet ground state (right). On the right side lie *spin orbitals*, each of which has a maximum occupation of one electron.

$\Delta E^x_{s-s} = 2.43$ eV und $\Delta E^x_{p-p} = 2.29$ eV, according to our spin-density-functional calculation (Appendix A).

The differential shielding of α and β electrons, due to the exchange hole, has consequences beyond the exchange splitting, since the spin orbitals associated with the different types of electrons have differing spatial extents (Figure 5). The low-lying α spin orbitals are more spatially contracted than the β spin orbitals. This graphical analysis can be made somewhat more quantitative by examining the compositions of the oxygen 2p atomic orbitals (AOs) and the positions of the maxima in their radial wavefunctions. Within the triple-ζ Slater-type orbital (STO) basis used in our calculations, the radial part of each AO ψ is expressed as a linear combination of three STOs (ϕ)[21] [Eq. (7)], where the individual STOs are defined by [Eq. (8)]

$$\psi^{2p} = \sum_{i=1}^{3} c_i^{2p} \phi_i^{2p} \tag{7}$$

$$\phi_i^{2p} = r e^{-\zeta_i^{2p} r} \tag{8}$$

For a numerical illustration, the expansion coefficients (c_i^{2p}) for the 2p AOs of both singlet and triplet oxygen are given in Table 1. The triplet $\psi^{2p}(\alpha)$ orbital has significantly larger contributions from the two more contracted basis functions (ϕ_2^{2p} and ϕ_3^{2p}) than triplet $\psi^{2p}(\beta)$. Conversely, $\psi^{2p}(\beta)$ has a larger contribution from the more diffuse ϕ_1^{2p}. The non-spin-

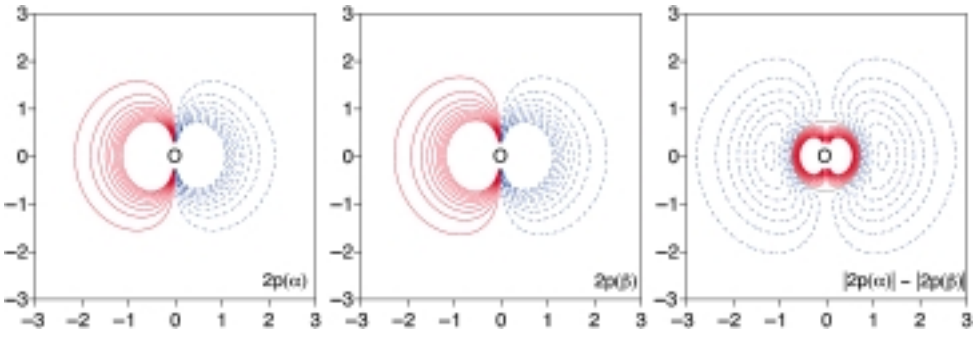

Figure 5. Contour plots of the 2p spin orbitals of triplet atomic oxygen: The left picture shows an α and the middle a β orbital. Since it is almost impossible to distinguish these from each other with the naked eye, the right pane shows an AO difference plot, the result of $|2p(\alpha)| - |2p(\beta)|$. In the AO plots the contours run from -0.1 to 0.1 in steps of 0.01; negative values are drawn with dashed lines. The contours in the difference plot run from -0.01 to 0.01 in steps of 0.001; negative values are drawn with dashed lines and the dotted line indicates the zero contour. All distances are in Å.

Table 1. Expansion coefficients (c) and locations of the maxima in the radial functions (r_{max}) for the 2p AOs of atomic oxygen. The orbital exponents of the STO basis functions (defined in [Eq. (8)]) are: $\zeta_1^{2p} = 1.12$, $\zeta_2^{2p} = 2.08$, $\zeta_3^{2p} = 4.08$.

	c_1^{2p}	c_2^{2p}	c_3^{2p}	r_{max} [Å]
Singlet $\psi^{2p}(\alpha,\beta)$	0.289	0.574	0.243	0.292
Triplet $\psi^{2p}(\alpha)$	0.255	0.602	0.245	0.284
Triplet $\psi^{2p}(\beta)$	0.348	0.528	0.239	0.307

polarized (singlet) AOs come somewhere in between the α and β values. Accompanying these changes is a shift in the positions of the radial maxima of the atomic orbitals: r_{max}(triplet $\psi^{2p}(\alpha)$) < r_{max}(singlet $\psi^{2p}(\alpha,\beta)$) < r_{max}(triplet $\psi^{2p}(\beta)$). Other light atoms behave in an analogous way.

To summarize, the exchange hole gives rise to a differential shielding of the α and β electrons of a spin-polarized system such that 1) the α/β electrons experience a higher/lower effective nuclear charge; 2) the α/β spin orbitals decrease/increase in energy; 3) they become less/more spatially diffuse relative to the non-spin-polarized system.

The above findings allow an easy interpretation of the work of Boyd, who concluded that the preference for a high-spin state in atoms (Hund's first rule) can be attributed to an increase in electron–nuclear attraction upon moving to the spin-polarized state.[22] Boyd's arguments run counter to the questionable textbook reasoning, stating that Hund's rule is due to a decrease in electron–electron repulsion in the high-spin state; rather, Hund's rule can be understood in terms of the foregoing differential shielding argument. In the triplet state, the electron–nuclear attraction in oxygen is stronger because the α electrons experience a higher effective nuclear charge; the β electrons experience a lower effective charge, but they are the minority. The electron–electron repulsion, on the other hand, *increases* since the α electrons are more spatially contracted and, on average, closer to each other.

3.3. Heavier Atoms

Upon moving down in the periodic table, the situation changes dramatically. For example, although both sulfur and selenium still exhibit a preference for the triplet state, their exchange splittings are considerably smaller: Moving down the group (O, S, Se), ΔE_{s-s}^{x} falls from 2.43 to 1.19 and finally to 0.91 eV and ΔE_{p-p}^{x} changes from 2.29 to 1.00 and then to 0.78 eV. In addition, the changes in the spatial extents of the orbitals are now much smaller (Figure 6). There is a significant decrease in the magnitudes of both the exchange splittings and the differences in spatial extent of the spin orbitals on moving from the first long row of the periodic table to the second and an additional, much smaller, decrease on moving from the second to the third.

We believe that the differences between the first and second long rows and the similarities between the second and third long rows can be understood in terms of the presence or absence of p orbitals in the nonvalence (core electron) region of the atom. Before presenting this explanation, which is very similar to that proposed by Kutzelnigg,[23] it is useful to briefly review the determination of the exponents of STOs.

Within Slater's original scheme[24] for determining the shielding of valence electrons by core electrons, the types of the core and valence orbitals[25] concerned were not taken explicitly into account. In fact, the 2s and 2p orbitals of oxygen have the same orbital exponent. In later work from Clementi and Raimondi, a series of fits of STOs in order to reproduce total atomic energies from numerical SCF calculations led to a modified version of Slater's rules.[26] In a less well-known publication, Burns presented yet another alternate formulation of Slater's rules.[27] Burns directly fitted STOs to atomic wavefunctions instead of trying to match the energies of these orbitals. Burns developed a different set of orbital exponents from those of Clementi and Raimondi, a set which is perhaps more reasonable for studying molecules since it treats the inner and outer parts of the wavefunction on more equal footing.[28] More importantly, Burns realized that a more effective set of rules for calculating STO shielding parameters could be produced by including the type of orbitals involved in the shielding expression. For example, using Burns's rules, a valence p electron is more effectively shielded by a core p electron than by a core s electron. The net result is that the 2p orbitals of oxygen are considerably more contracted (reduced shielding produces a larger exponent) than the 2s orbital since there is no 1p orbital within the core. This result is, of course, very well known within pseudopotential theory: The first instance of a particular type of orbital (such as 2p, 3d, 4f) is always quite contracted.

Since the 2p orbitals of oxygen atoms are more contracted than either the 3p orbitals of sulfur or the 4p orbitals of selenium, the p electrons of oxygen spend considerably more time close to the nucleus than those of either sulfur or selenium. Consequently, small changes in the shielding of the oxygen 2p electrons, such as those caused by spin polarization, must have a larger impact than they do for the 3p or 4p electrons. The net result is that the perturbations caused by the transition to the triplet state in sulfur are smaller than those in oxygen. The perturbations for selenium, which has two p shells in the core, are even smaller.

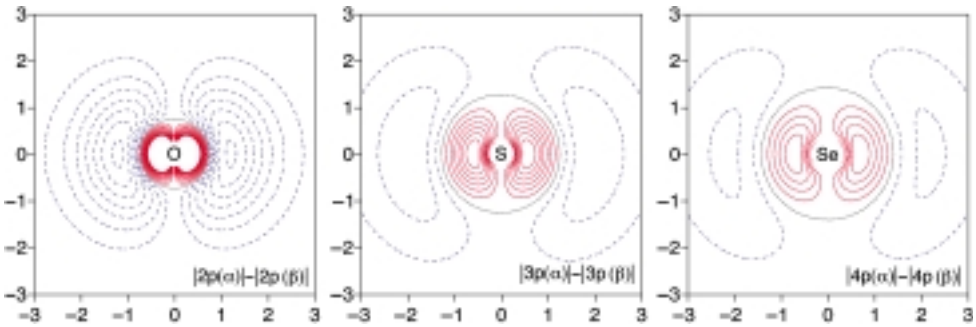

Figure 6. AO difference plots for the p orbitals of triplet-state atoms O (left), S (center), and Se (right). The contours and line patterns are the same as those in the right pane of Figure 5.

3.4. Diatomic Molecules

The same arguments about the exchange hole and shielding used above for atoms also apply to molecules with unpaired electrons. For example, the energy levels of O_2 change in an exactly analogous way to those of atomic oxygen when the molecule changes from a singlet to a triplet state (Figure 7). Focusing only on the HOMO—the antibonding $2\pi(\pi^*)$ orbital—the exchange splitting in O_2 ($\Delta E^x_{2\pi-2\pi}$) is 1.85 eV. Moving down to S_2 and Se_2, $\Delta E^x_{2\pi-2\pi}$ falls to 0.81 and 0.63 eV, respectively. The exchange splitting decreases upon moving down the group.

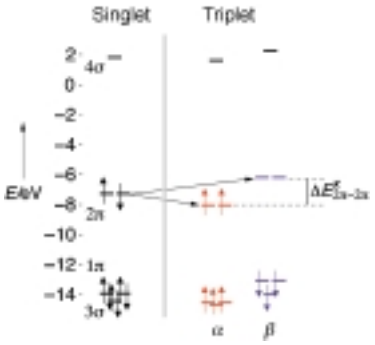

Figure 7. Energy level diagrams for molecular oxygen in the singlet excited state $^1\Delta_g$ (left) and in the triplet ground state $^3\Sigma_g^-$ (right).

The α and β spin orbitals of triplet Q_2 (Q = O, S, Se) show the same behavior and trends as those in triplet Q (Figure 8). The 2π spin orbital of the majority spin species (α) is more contracted than that of the minority species (β). The differences in both exchange splittings and spatial extents of the $2\pi(\alpha)$ and $2\pi(\beta)$ spin orbitals are again larger upon moving from first to second row ($O_2 \rightarrow S_2$) than from second to third ($S_2 \rightarrow Se_2$).

One final word about the molecular results before considering the solid state. In all three diatomic molecules discussed above, the process of spin polarization increases the splitting between the highest-occupied molecular orbital (HOMO) and the lowest-unoccupied molecular orbital (LUMO).[29] This energy difference may be interpreted in the context of the theory of chemical hardness,[30] which is intimately connected with questions of chemical reactivity. In fact, density-functional theory reveals that the chemical hardness η of a molecule may be defined by Equation (9)[31]

$$\eta = \frac{E_{\mathrm{LUMO}} - E_{\mathrm{HOMO}}}{2} \tag{9}$$

It is noteworthy that O_2, S_2, and Se_2 all become chemically *harder* (less reactive) by a few percent upon changing from the singlet excited state to the triplet ground state. The decrease of their total energies is parallel to an increase in their chemical hardness upon a distortion; in this case an electronic distortion. This effect fits nicely into the principle of maximum hardness: In general, more stable species are chemically harder.[30]

4. Ferromagnetism in the Elemental Transition Metals

"Es geht auch anders,
doch so geht es auch."[*][32]

4.1. The Phenomenon

Though transition metal atoms are paramagnetic in the gas phase, only a few exhibit cooperative magnetism, such as ferromagnetism, in the solid state (Figure 9). The only "magnetic" transition metals occur close to the end of the first transition series. Metals Fe, Co, and Ni are all ferromagnetic, whereas Cr and Mn have antiferromagnetic ground states. Let us initially limit our attention to the ferromagnetic metals as the antiferromagnetic structures of Cr (incommensurate spin-density waves) and Mn (with 58 atoms in the magnetic unit cell) pose computational difficulties. It is obvious from Figure 9 that ferromag-

Sc	Ti	V	Cr	Mn	Fe	Co	Ni	Cu
hcp	hcp	bcc	bcc	X	bcc	fcc	fcc	fcc
Y	Zr	Nb	Mo	Tc	Ru	Rh	Pd	Ag
hcp	hcp	bcc	bcc	hcp	hcp	fcc	fcc	fcc
La	Hf	Ta	W	Re	Os	Ir	Pt	Au
hcp	hcp	bcc	bcc	hcp	hcp	fcc	fcc	fcc

Figure 9. A section of the periodic table showing the structures and magnetic properties of the transition metals. Elements with yellow backgrounds are antiferromagnetic, while those with orange-red backgrounds are ferromagnetic. The abbreviations for the structures are: hcp: hexagonal close packed; bcc: body-centered cubic; fcc: face-centered cubic; X: the α-Mn structure type.

[*] *"There are other ways, but this one's fine, too."*

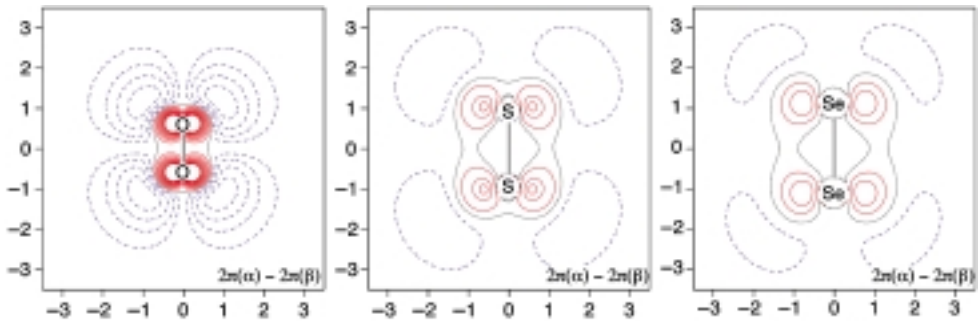

Figure 8. Molecular orbital difference plots for the $2\pi(\pi^*)$ orbitals of triplet O_2 (left), S_2 (center), and Se_2 (right). The contours and line patterns are the same as those in the right pane of Figure 5.

netism is not solely a consequence of structure or electron count. For example, Pt and Pd both adopt the same face-centered cubic (fcc) structure and have the same number of valence electrons as Ni, yet neither is ferromagnetic. Ferromagnetism clearly arises from a set of special electronic circumstances.[4]

In order to understand these circumstances, we adopt the view that the nonmagnetic state is "normal" in the solid and ferromagnetism is an unusual phenomenon. Using this approach, we will come to ferromagnetism by first understanding why most elemental metals are not ferromagnetic. This can be most directly achieved by drawing an analogy with molecular complexes of the transition metals and their ions.

Hund's first rule states that the most stable form of free atoms or ions is the high-spin state; a d^6 transition metal ion has preferentially four unpaired electrons (Figure 10a). When we introduce a perturbation by a set of ligands with an octahedral coordination, the degeneracy of the d orbitals is

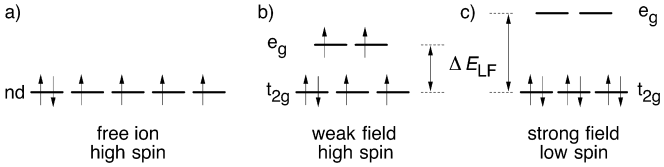

Figure 10. Energy-level diagrams and electronic configurations for the d orbitals of: a) a free d^6 transition metal ion; b) a d^6 transition metal ion with an octahedral environment of weak-field ligands; c) a d^6 transition metal ion with an octahedral environment of strong-field ligands. For simplicity, we limit ourselves to the one-electron picture, neglect spin–orbit coupling, and ignore the spherical energetic part of the ligand field.

broken and they split into t_{2g} and e_g sets. If the metal–ligand interactions are weak and the perturbation is small (Figure 10b), then the splitting between e_g and t_{2g} (ΔE_{LF}) is also small; the six electrons fill the energy levels in a high-spin arrangement just as in the free ion. If the metal–ligand interactions are strong and the perturbation is larger (Figure 10c), then ΔE_{LF} is also large enough so the electrons form pairs in the t_{2g} orbitals and the complex is nonmagnetic. One could say that the strong ligand field has totally quenched the magnetism of the free ion.

The situation is similar in the elemental structures of the transition metals: The magnetism of the free atoms is quenched when those atoms are condensed into a crystal. Like many other concepts in the band theory of solids, this is most easily illustrated using a simple model: a one-dimensional chain of hydrogen atoms (Figure 11). A free hydrogen atom is, of course, Curie paramagnetic, with one electron sitting unpaired in an s orbital. When we form a one-dimensional chain, the energy levels of the atoms spread out to form a band. If the interactions between the atoms in the chain are weak (a small perturbation), then the resulting band, ΔE_{BW}, is narrow and each crystal orbital is half-filled (Figure 11a). This is the crystalline equivalent of the weak ligand-field case (Figure 10b). A large perturbation (strong interactions between the atoms in the chain) results in all the electrons pairing (Figure 11b). The magnetism of the free atoms is quenched in the crystal when the interatomic interactions, and thus bandwidths, are large.

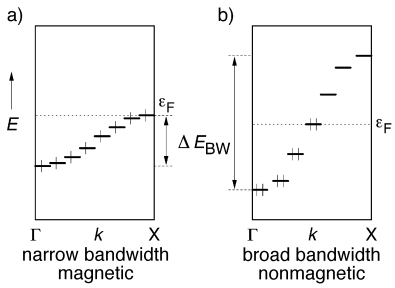

Figure 11. Qualitative band structures and electron fillings for a one-dimensional chain of hydrogen atoms with: a) narrow bandwidth (weak H-H interactions) and b) broad bandwidth (strong H-H interactions).

The rare-earth elements typically display the narrow-bandwidth magnetism sketched in Figure 11a. The majority of the interatomic bonding in these metals is mediated through the 5d and 6s electrons. The 4f orbitals, which are strongly spatially contracted, are only slightly perturbed by the neighboring atoms and give rise to very narrow bands. The localized-electron magnetism of the rare-earth metals is characterized by magnetic moments which approach those in the free atoms and by complicated magnetic structures.[33] The origin of this localized-electron magnetism is reasonably easy to understand: The f bands are so narrow that the energetic cost associated with populating the entire band with electrons is small compared to the cost associated with pairing the electrons.[34] Consequently, the band is filled, in a manner analogous to the configuration of atomic energy levels following Hund's rule, and results in unpaired spins and magnetic moments. What is considerably more difficult to understand is what determines the structure adopted by those unpaired f electrons. The magnetic structures of the rare earths run the gamut from the simple ferromagnetism observed in gadolinium to the sinusoidal spin structures of erbium and terbium.[33]

As localized-electron magnetism is not our focus here, we leave this complicated story and return to itinerant-electron ferromagnetism in the transition metals. In these metals, the d orbitals contain the electrons responsible for magnetism. However, in contrast to the f orbitals of the rare-earth elements, transition metal d orbitals are involved in strong interatomic interactions. This gives rise to fairly broad bands in the elemental transition metals. Figure 11b is a more appropriate model of their bands than Figure 11a. Consequently, most elemental transition metals are non-magnetic.

4.2. Itinerant (Delocalized) Electron Ferromagnetism

The changes to the electronic structure of a system with broad bands which allow ferromagnetism are best introduced using qualitative density of states (DOS) plots.[35] In Figure 12a, the DOS of a nonmagnetic metal is sketched as a rectangular block, divided into boxes to allow states to be counted. The same DOS is shown in a spin-resolved way (where the α and β states are plotted separately) in Figure 12b. The occupations of the α and β spin sublattices, determined by counting the number of boxes lying below the

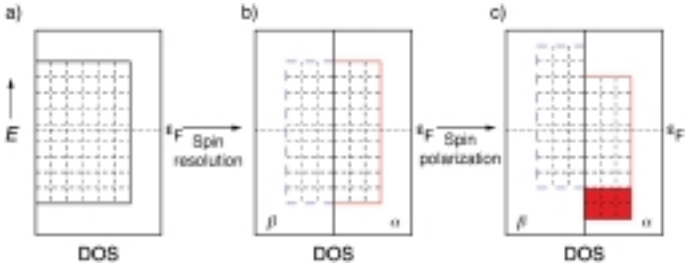

Figure 12. Qualitative DOS curves for a transition metal. a) The DOS of a nonmagnetic metal. b) Spin-resolved form of the same DOS (DOS for α and β electrons are drawn separately). c) Shifts in the α and β spin sublattices upon the onset of magnetism (spin polarization). The red-shaded region indicates the "excess" α spins. In all three panes, the horizontal dotted line indicates the position of the Fermi level (ε_F). The grid superimposed on the DOS curves facilitates the counting of states.

Fermi level (ε_F), are identical. When this system becomes magnetic, the α and β DOS curves change in energy: The α/β spin sublattice moves down/up (Figure 12c). Since the two sublattices must share a common Fermi level, the net result of this spin polarization is a higher occupation of the α states. The number of "excess" α states, and thus the permanent magnetic moment of the system, can be determined by counting the number of boxes in the red-shaded region of Figure 12c.

Notice the strong similarities, on moving from the low- to the high-spin configuration, between the DOS of a solid becoming magnetic and the changes in the energy-level diagrams of atoms (Figure 4) and molecules (Figure 7). In each case the states (energy levels) associated with the α electrons (the majority spin species) decrease in energy relative to the nonmagnetic case while the β energy levels increase. In this respect, itinerant-electron ferromagnetism is not so different from atomic and molecular magnetism. As we shall demonstrate later, the similarities run even deeper than the shifts in energy levels.

4.3. The Archetype: Iron

We begin our examination of ferromagnetism in the transition metals with a detailed analysis of the archetypical ferromagnet: body-centered cubic (bcc) iron (α-Fe). In α-Fe each iron atom is surrounded by eight nearest neighbors, in a cubic arrangement, at a distance of 2.485 Å and six next-nearest neighbors, in an octahedral arrangement, at a distance of 2.870 Å (Figure 13). Below its Curie temperature (T_c = 1044 K) α-Fe is ferromagnetic, with a saturation magnetic moment of 2.21 μ_B.[33]

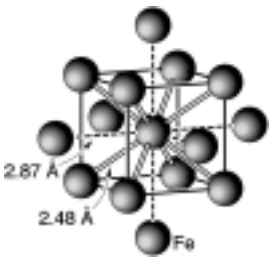

Figure 13. The coordination environment of iron in the bcc α-Fe structure.

We start with the electronic structure of an Fe phase which does not exist: *nonmagnetic* bcc Fe. This is not a model of Fe above T_c, which has a different lattice constant and significant (albeit short-range) magnetic order.[36] The calculated band structure, the DOS and Fe-Fe crystal-orbital Hamilton population (COHP) curves for this phase, are presented in Figure 14. The computational methodology is explained in Appendix A. At most high-symmetry points in the first Brillouin zone (BZ), which is shown in

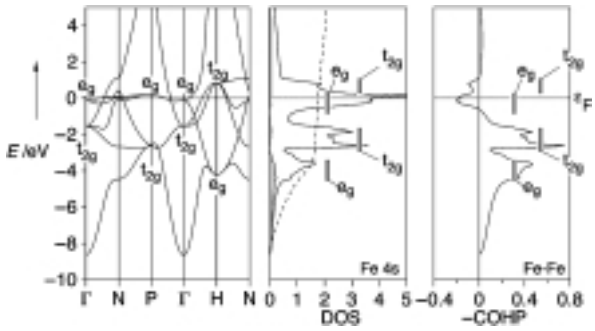

Figure 14. Band structure (left), DOS, and Fe-Fe COHP curves for nonmagnetic α-Fe. The shaded region and dashed line in the DOS curve corresponds to the projected DOS of the Fe 4s orbital and its integration, respectively. All curves have been shifted in energy so that ε_F, indicated with a horizontal dotted line, lies at 0.0 eV.

Figure 15, the crystal orbitals which arise from the Fe 3d block split into two sets: triply degenerate t_{2g} and doubly degenerate e_g; the point-group irreducible representation labels used here are those appropriate for the cubic point symmetry of the Fe atoms. Labeling the bands in this manner allows us to roughly characterize the peaks in the DOS and COHP curves to their orbital composition. The primarily e_g crystal orbitals are mostly flat (exceptions of $\Gamma \rightarrow H$ and $H \rightarrow N$) whereas the t_{2g} orbitals show reasonable dispersion along every symmetry direction. We can understand this disparity by considering the shapes of the crystal orbitals, sketched at the symmetry points Γ and N in Figure 16. The t_{2g} orbitals are pointed more directly at the nearest-neighbor atoms (which lie on the corners of the cube in this Figure). These orbitals have π symmetry with respect to the more distant next-nearest neighbors at the ends of the dashed lines. The e_g orbitals, involved in σ interactions with the next-nearest neighbors, are not oriented particularly well for nearest-neighbor interactions. The symmetry line from $\Gamma \rightarrow H$ lies along one of the Cartesian reciprocal axes (Figure 15), therefore motion along this line strongly affects next-nearest-neighbor interactions and gives rise to a large e_g bandwidth from Γ to H. The nearest-neighbor interactions are affected along all directions, therefore the t_{2g} orbitals show a significant bandwidth along every symmetry line.

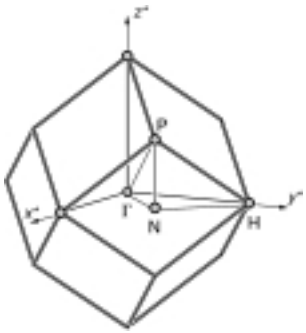

Figure 15. The first Brillouin zone for a bcc lattice with high-symmetry points labeled. The vectors x^*, y^*, and z^* are Cartesian reciprocal axes.

Continuing our analysis of Figure 14, we observe the three-peaked DOS typical of bcc metals. As is true for all transition metals, the s band penetrates the d block to yield s-dominated

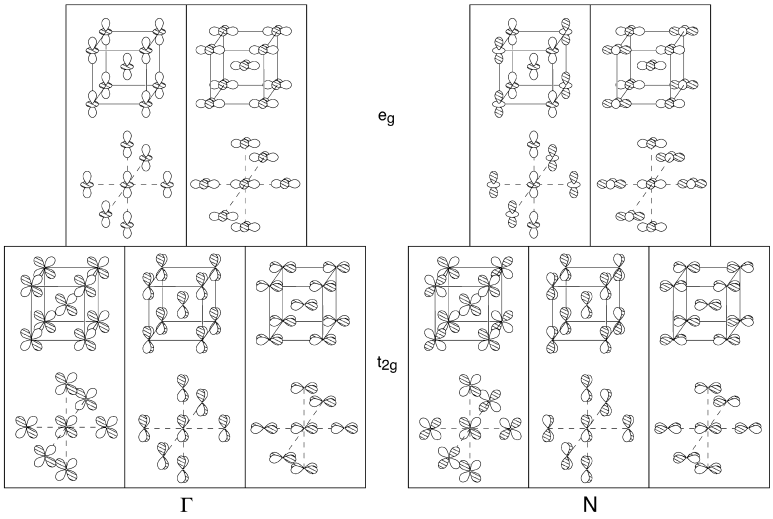

Figure 16. Iconic representations of the crystal orbitals of α-Fe at the high-symmetry points Γ and N. Each orbital is drawn in two parts: one showing nearest-neighbor contacts, the other next-nearest-neighbor contacts. The t_{2g} and e_g labels, strictly valid in Γ, are used only to qualitatively group orbitals in N.

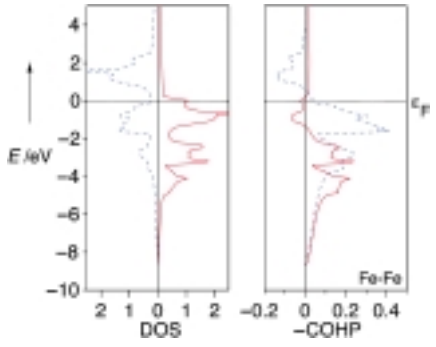

Figure 17. DOS and Fe-Fe COHP curves for ferromagnetic α-Fe. In each plot, the solid red/dashed blue line corresponds to the α/β spins. All curves have been shifted in energy so that ε_F, indicated with a horizontal dotted line, lies at 0.0 eV.

states at the base of the DOS. Up to this point, we have encountered nothing unusual in the electronic structure of hypothetical nonmagnetic α-Fe. The first indication that something is wrong appears in the Fe-Fe COHP curve.

As we would expect, the low-energy end of the DOS, that is primarily composed of s states, is Fe-Fe bonding. This is followed by two Fe-Fe bonding peaks. The first, between -3 and -5 eV, mostly arises from the e_g orbitals. The second, between -3 and -1 eV, mainly has a t_{2g} character. Of these two peaks, the one from the t_{2g} set is more strongly bonding between nearest neighbors, as we anticipate based upon the discussion above. In the next-nearest-neighbor COHP curve (not shown here), the e_g states are significantly more strongly bonding between next-nearest neighbors; again, fitting our expectations. The integrated Fe-Fe COHPs (ICOHPs) are -1.448 and -0.683 eV per bond for the nearest-neighbor and next-nearest-neighbor interactions, respectively. The curious thing about the electronic structure of nonmagnetic α-Fe is that ε_F falls in a strong Fe-Fe *antibonding* region. Normally, the appearance of ε_F in strongly antibonding states is an alarm that indicates a system is unstable with respect to some sort of structural change. However, we know that Fe does not undergo any such distortion and that the bcc structure is stable. How are we to understand this? The answer is that α-Fe *does undergo a distortion* but instead of the atoms of the structure rearranging themselves, the *electrons* do. Nonmagnetic α-Fe is unstable with respect to an electronic structure distortion, which makes the α and β spin sublattices inequivalent (thereby reducing the electronic symmetry), lowers the energy, and gives rise to ferromagnetism.

When a spin-polarized calculation is performed for bcc Fe, the two spin sublattices become inequivalent and shift in energy (Figure 12c). This results in different populations of the α and β sublattices and a calculated spin magnetic moment of 2.27 μ_B, very close to the experimental value of 2.21 μ_B. The total energy decreases by 0.43 eV upon spin polarization. The spin-polarized DOS and Fe-Fe COHP curves of ferromagnetic α-Fe are shown in Figure 17. The α and β DOS curves in Figure 17 are very similar to each other and to the nonmagnetic DOS in Figure 14: Spin-polarization has *not* significantly affected the shape of the DOSs; merely shifted them in energy. While the α spin sublattice has decreased in energy enough to almost completely fill the d block, the β spins have increased to maintain a constant number of electrons in the system as a whole. The shift of the primarily s states (at the base of each DOS curve) is quite small—the s orbitals are not significantly affected by the onset of ferromagnetism. Moving our focus to the chemical bonding in magnetic Fe, the α and β COHP curves are similar in shape but differ in size. Firstly, the α COHP curve is quite a bit smaller in magnitude than its β counterpart. Secondly (and equally important), the shifts in the two curves have removed the Fe-Fe antibonding states from the vicinity of ε_F. The integrated Fe-Fe COHPs for the α and β electrons are -0.552 and -0.975 eV per bond and a total ICOHP of -1.527 eV per bond. The onset of ferromagnetism has *strengthened* the Fe-Fe nearest-neighbor bonds by more than 5%, parallel to the decrease in the total energy.

As expected, spin-polarization results in a rearrangement of the electron density in α-Fe. The nature of the electron density shifts are shown in Figure 18 by plotting the quantity $\Delta\rho = \rho(\text{magnetic}) - \rho(\text{nonmagnetic})$ evaluated in a plane

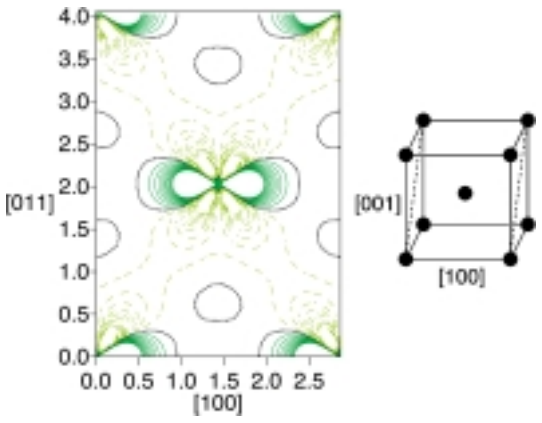

Figure 18. Changes in the electron density of α-Fe upon spin polarization. Solid green curves indicate positive values (higher electron density in the magnetic state) and dashed yellow curves negative (lower electron density in the magnetic state); the dotted black lines are the zero contours. The location of the plane in the unit cell is sketched on the right.

containing both nearest-neighbor and next-nearest-neighbor contacts. In nonmagnetic bcc Fe, the states at and just below ε_F are antibonding between nearest neighbors; these regions lie along the diagonal of the plot in Figure 18. These states are depleted in the magnetic form, to result in a shift of electron density out of the spatial regions between nearest neighbors. The "lost" electron density accumulates in the areas between next-nearest neighbors.

As mentioned above, the energy shifts of the α and β spin sublattices in ferromagnetic Fe mirror those of the atomic/molecular orbitals of O/O_2 (Figures 4 and 7). These shifts are once again a consequence of the exchange hole. The majority spin species (α) is not as effectively shielded from the nucleus as in the nonmagnetic "phase", so the α states decrease in energy. The β states, on the other hand, experience better shielding and increase in energy. We would expect that these changes give rise to differences in the spatial extents of the two sets of states as well. This effect is indeed present and responsible for the different sizes of the α- and β-COHP curves. The more spatially contracted α states are not as strongly Fe-Fe bonding as the β states, which have become more diffuse. The differing spatial extents of the spin-sublattices is one of the major factors contributing to the fact that the nearest-neighbor β ICOHP is almost twice as large as the α ICOHP (see above). The fact that almost the entire α d block is occupied, including the Fe-Fe antibonding states at the top, also plays a large role. The α ICOHP, which was smaller than β to start with due to the spatial contraction of the α spin orbitals, is weakened further by the population of antibonding states, in contrast to those of the β spin sublattice which lie above ε_F. Despite the weaker α interactions, the strengthening of the nearest-neighbor interactions in the β sublattice is sufficient to result in an ICOHP value for ferromagnetic Fe larger than that for the nonmagnetic structure.

We can also demonstrate the differential spatial extents of the α and β spin sublattices by a plot similar to those of Figures 6 and 8. Within the linear muffin-tin orbital (LMTO) calculations, the electron density is the only physically meaningful quantity accessible. However, since the α and β sublattices contain different numbers of electrons, a straightforward plot of $\rho(\alpha)-\rho(\beta)$ does not contain the sought information; rather, this result gives the spin density and shows where in real space the electrons responsible for magnetism are located. In order to see the differences in the spatial extents of the α and β electron densities, we must scale either one or both of them in order to equalize the effective numbers of electrons they contain. Figure 19 shows such a plot, namely of the scaled quantity of Equation (10), where n_α and n_β are the total number of electrons in the α and β spin sublattices (5.135 and 2.865, respectively).

$$\frac{n_\beta}{n_\alpha}\rho(\alpha)-\rho(\beta) \qquad (10)$$

Just as the α AOs/MOs of O/O_2 were more spatially contracted than the corresponding β AOs/MOs, the α electron density of ferromagnetic Fe is greater near the nucleus, whereas the β electron density is greater in the regions further away from the nuclei, particularly around the nearest-neighbor contacts.

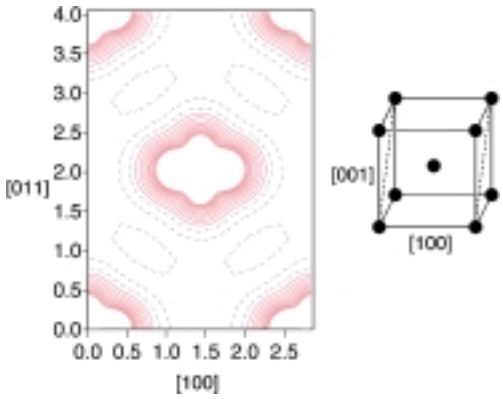

Figure 19. Scaled electron-density difference (defined in [Eq. (10)]) in α-Fe evaluated in the (011) plane of the cubic unit cell. Solid red curves indicate positive values (regions where α spins are dominant), dashed blue curves negative (β spins dominant). The location of the plane in the unit cell is sketched on the right.

Though the similarities in the electronic structural changes on the transition from low- to high-spin states in atoms and molecules were not unexpected, it is rather surprising how analogous the situation is for itinerant-electron ferromagnetism. Spin polarization causes differential shielding of the majority and minority spin species. Majority (α) electrons see a larger nuclear charge, decrease in energy, and become more spatially contracted. The β electrons, better shielded from the nuclear charge by the α electrons, increase in energy and become more diffuse.

Before closing the iron section, we would like to comment on the localized/delocalized antagonism in the understanding of transition-metal ferromagnetism. The alert reader might have noticed that we have started by using a fairly localized basis set—the short-ranged, tight-binding, linear muffin-tin orbitals (TB-LMTO)—in order to generate totally delocalized crystal orbitals (Bloch functions) that spread over the entire crystal. In the spirit of Stoner's ideas, the valence electrons responsible for ferromagnetism in iron are also completely delocalized.

Our interpretation of itinerant-electron ferromagnetism as an essentially chemical phenomenon retrieves the localized picture from the delocalized wave functions. The driving force for ferromagnetism lies in the *local* antibonding character of the states around ε_F. It comes as no surprise to realize that the strength of the covalent bonding interactions between Fe atoms decays rapidly with interatomic distance. For example, the nearest-neighbor bonds (2.485 Å, ICOHP = – 1.527 eV) in α-Fe are significantly stronger than the next-nearest-neighbor bonds (2.870 Å, ICOHP = – 0.658 eV). When these two energies are related using a simple distance power law—as done for the molecular field by Weiss—an exponent of 5.8 arises, almost coincident with Weiss's experimental exponent of 6.0. In our view, there is a *local* source for the delocalized ferromagnetism.

4.4. Cobalt and Nickel

α-Fe is, of course, only one of the three ferromagnetic transition metals. When we go from Fe to Co or Ni, in addition

to increasing the number of valence electrons, the structure itself changes from bcc to fcc. This structural change alters the shapes of the DOS and COHP curves and the presence of additional d electrons moves ε_F up in both curves. Although the crossover point from bonding to antibonding in the M-M COHP curve of the fcc structure comes somewhat later than that in the bcc structure (discussed in greater detail below), the presence of the extra d electrons raises ε_F enough such that it lies in strongly antibonding states. Once again there is a driving force for the onset of magnetism, and the spin polarization process results in a net stabilization.

The spin-polarized DOS and COHP curves of ferromagnetic Ni (calculated $\mu = 0.62\,\mu_B$, precisely matching the experimental value), shown in Figure 20, displays features similar to those of Fe (Figure 17). Whereas the α states

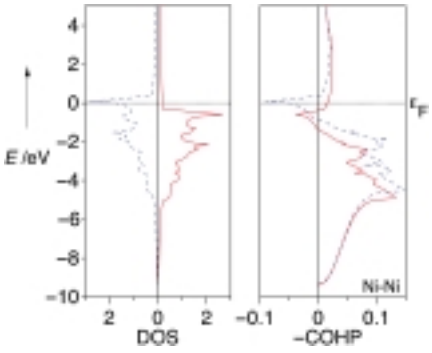

Figure 20. DOS and Ni-Ni COHP curves for ferromagnetic Ni. In each plot, the solid red/dashed blue line corresponds to the α/β spins. All curves have been shifted in energy so that ε_F, indicated with a horizontal dotted line, lies at 0.0 eV.

decrease in energy and are filled to just above the top of the d block, the β states increase in energy and the d block is partially empty. The contracted α states are involved in weaker interactions between nearest neighbors than the more diffuse β states. The difference in energies between the two spin sublattices (the exchange splitting) is smaller for Ni than for Fe, as is the size difference between the two COHP curves. The reason the α and β spin sublattices are so similar is the magnetic moment of Ni ($0.62\,\mu_B$) is quite small when compared to that of α-Fe ($2.27\,\mu_B$). The similarly small resulting differential-shielding effects are reflected in small exchange splittings and little difference in the spatial extents of the α and β spin sublattices. The magnetic moment in Ni is so small because the 3d block is almost full—there is insufficient room to accommodate a significant excess of α states. In keeping with the small magnetic moment and little difference between the α and β sublattices, the increase in the Ni–Ni bond strength with the onset of magnetism is only about half a percent: the Ni-Ni ICOHP increases from -0.991 to -0.996 eV per bond.

As we expect, Co, with its calculated magnetic moment of $1.60\,\mu_B$ (experimental value: $1.74\,\mu_B$[33]), lies somewhere in between Fe and Ni. The differences between the α and β DOS and COHP curves (not shown) are smaller than those in Fe but larger than in Ni. The Co-Co ICOHP increases from -1.177 to -1.224 eV per bond upon spin-polarization, or about 4%.

To recap, Co and Ni show behavior similar to that of α-Fe, but to a lesser degree:

1. In the nonmagnetic calculations, ε_F falls in a region of significant M-M antibonding.
2. Spin polarization results in the α/β levels decreasing/increasing in energy.
3. Spin polarization leads to differing spatial extents of the α and β spin sublattices: α becomes more contracted while β becomes more diffuse.
4. Spin polarization removes M-M antibonding levels from the vicinity of ε_F.

4.5. Other 3d Transition Metals

The discussion has led us to a point where we can comfortably assert that ferromagnetism is associated with the presence of M-M antibonding states at ε_F. This assertion is easily tested by examining the M-M COHP curves for the entire first transition series. These are presented, along with the corresponding DOS curves, in Figure 21. All calculations

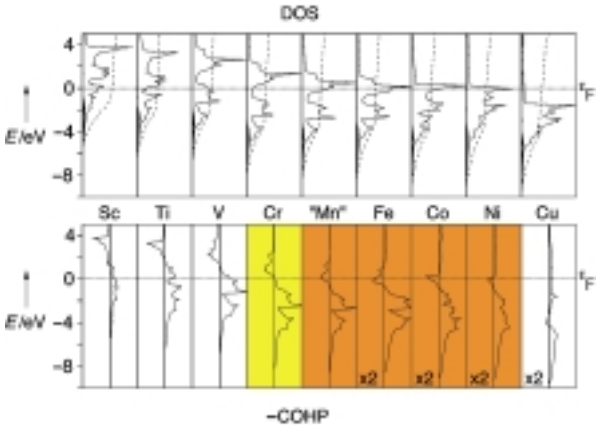

Figure 21. Non-spin-polarized DOS (top) and M-M COHP curves (bottom) for the first-row transition metals. The electronic structure of Mn was calculated in a bcc structure with a lattice constant of 2.88 Å. The shaded area in each DOS curve indicates the contribution of the M 4s states. All curves are on the same horizontal and vertical scales except for the M-M COHPs in Fe, Co, Ni, and Cu, which have been multiplied by a factor of two. The curves have been shifted in energy so that ε_F, indicated with a horizontal dotted line, lies at 0.0 eV.

were carried out using the experimental structures of the metals (taken from ref. [37]) with the exception of manganese. The 29 atom crystallographic unit cell of α-Mn does not lend itself to high-level electronic structure calculations well, so we need a simplifying model. Since both the neighbors of Mn in the periodic table (Cr and Fe) adopt bcc structures, we use here a bcc structure with a lattice constant halfway in between those of Cr and Fe (2.88 Å). The density of the structure by this model is only 2% lower than that of α-Mn itself. We will refer to this pseudo-manganese structure as "Mn". All calculations in Figure 21 were carried out in a non-spin-polarized mode.

In the early transition metals, such as Ti, ε_F is low enough in the COHP curve that it falls in a region of M-M bonding. In

the early transition metals there is thus no driving force for ferromagnetism! By Cr, ε_F has moved up far enough in the COHP curve that it occurs at the crossover point between bonding and antibonding. The nonbonding nature of the states at ε_F in Cr may well be responsible for the observed spin-density-wave antiferromagnetism, but we will not examine that in detail here. From "Mn" to Ni, ε_F lies in states which are clearly M-M antibonding. As we know, Fe, Co and Ni are all ferromagnetic, and our calculations predict that "Mn", if it existed at low temperatures, would also be ferromagnetic; the calculated moment is 0.99 μ_B.[38]

These results seem quite straightforward and clear: the presence of M-M antibonding states at ε_F in the nonmagnetic electronic structure of a transition metal is a sign that indicates this metal would "prefer" to be ferromagnetic. We believe that these M-M antibonding states are not only indicative of an instability with respect to spin polarization, but also that they are *causative*. That is, the antibonding interactions are actually responsible for the instability and drive the system to ferromagnetism.

4.6. Iron Revisited: the Face-centered Cubic Phase

Before examining the second- and third-row transition metals, there is a legitimate question on the first-row metals to answer: Why is the face-centered cubic phase of iron not ferromagnetic?

In order to facilitate comparison with the α-Fe results, we have chosen to calculate the electronic structure of fcc Fe with a lattice constant of 3.51 Å. This gives Fe-Fe nearest-neighbor distances identical to those in α-Fe. While this is admittedly an underestimation of the lattice constant (the bond lengths for the twelve coordinate fcc structure should be larger than those in the eight-plus-six coordinate bcc structure), it does allow direct comparison of the relative Fe-Fe bond strengths in the two structures. The DOS and Fe-Fe COHP curves for fcc Fe with this lattice constant are shown in Figure 22. Clearly, the shape of the DOS of fcc Fe is considerably different from that of α-Fe (Figure 14). The characteristic three-peaked bcc DOS has been replaced with the considerably more uniform DOS typical for fcc metals (compare too with the DOS curves for Ni and Cu in Figure 21). In addition, ε_F no longer lies in a strongly antibonding peak in the COHP curves! In this fcc structure ε_F lies on the weakly antibonding shoulder of the Fe-Fe antibonding states. The Fe-Fe ICOHP is -1.519 eV per bond, intermediate between those of nonmagnetic and magnetic α-Fe. Since the number of electrons is the same in the bcc and fcc structures, the antibonding COHP peak lying above ε_F implies that the crossover point from bonding to antibonding in the fcc structure has been shifted to higher electron filling. Face-centered cubic iron is not ferromagnetic because the states around ε_F are only weakly antibonding—the driving force for ferromagnetism is just not strong enough. In fact, the almost nonbonding character of the states around ε_F reminds us strongly of the bonding situation in Cr, which is antiferromagnetic. Further: when embedded in a Cu matrix, fcc Fe is known to be antiferromagnetic at low temperatures,[39, 40] leading us to expect that bulk fcc Fe would also be antiferromagnetic if it were stable at low temperatures. The presence of ε_F in a region of nonbonding states may well be a sign for antiferromagnetism.

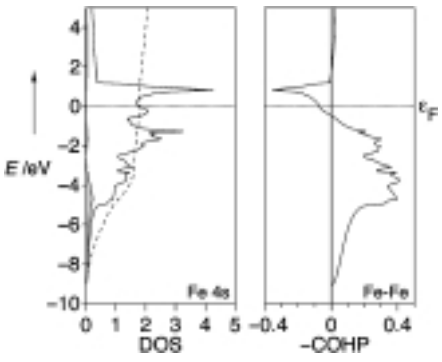

Figure 22. DOS and Fe-Fe COHP curves for nonmagnetic fcc Fe. The shaded region and dashed line in the DOS curve corresponds to the projected DOS of the Fe 4s orbital and its integration, respectively. All curves have been shifted in energy so that ε_F, indicated with a horizontal dotted line, lies at 0.0 eV.

In order to make fcc Fe ferromagnetic, ε_F must be moved into the strongly M-M antibonding states by adding more electrons to the system. This is precisely what happens in iron-rich fcc alloys, such as Fe_3Pd, to be discussed later.

4.7. The 4d and 5d Transition Metals

There is another question about ferromagnetism in the transition metals: Why does it only appear in the first row? For example, why are palladium and platinum, which have the same structure and same number of valence electrons as nickel, not ferromagnetic?

It is reasonable to assume that the second- and third-row transition metals have COHP curves similar in shape to those of the corresponding first-row elements. This assumption was confirmed by a series of calculations (not shown here). The early transition metals of the second and third rows are very similar to those of the first row: ε_F lies in M-M bonding states low in the COHP curve and there is no driving force for magnetism. However, at the end of a series, we would expect ε_F to lie in the antibonding levels at the top of the d block. For example, given that Pd and Pt are both isostructural and isoelectronic (referring only to the number of valence electrons) to Ni, this qualitative analysis leads to the tentative prediction that Pd and Pt should be ferromagnetic. This is, evidently, not the case. To explain this puzzle, we shall focus our attention on Pd; similar arguments apply to all other late second- and third-row metals.

The DOS and Pd-Pd nearest-neighbor COHP curve for elemental Pd is shown in Figure 23. As we predicted above, ε_F falls in a region of Pd-Pd antibonding, just as it did in Ni. In fact, aside from the somewhat broader and more uniform d block, the electronic structure of Pd is very similar to that of Ni (Figure 21). It seems like Pd should be ferromagnetic.

In order to understand why Pd is more stable in a nonmagnetic state, it is most convenient to computationally force it into a ferromagnetic state and see why that state is unstable. However, any reliable, self-consistent, spin-polar-

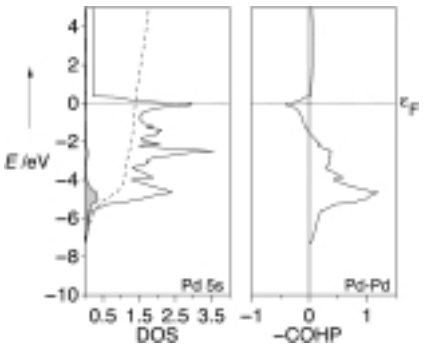

Figure 23. DOS and Pd-Pd COHP curves for Pd. The shaded region and dashed line in the DOS curve corresponds to the projected DOS of the Pd 5s orbital and its integration respectively. All curves have been shifted in energy so that ε_F, indicated with a horizontal dotted line, lies at 0.0 eV.

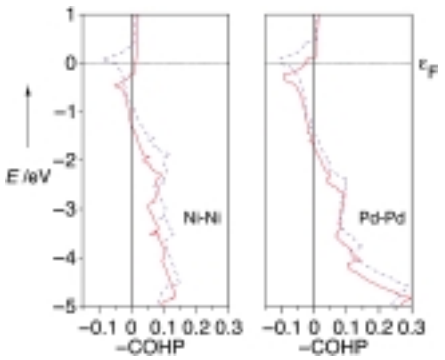

Figure 24. The M-M COHP curves of spin-locked ($\mu \equiv 0.5\,\mu_B$) Ni (left) and Pd (right) within a small energy window around ε_F. In each pane the solid red/dashed blue line corresponds to the α/β spins. All curves have been shifted so that $\varepsilon_F = 0.0$ eV.

ized calculation of the electronic structure of Pd which starts from a magnetic state will eventually shed the magnetic moment and become nonmagnetic. A straightforward trick to overcome this problem is to start from the self-consistent potential for nonmagnetic Pd, set the magnetic moment of Pd to some small number, and carry out a single iteration of the self-consistency cycle. This is not an optimal solution, simply because the frozen potential here does not correspond to the magnetic state. We solve this problem by carrying out what we call *spin-locked* calculations. Starting from the potential of the nonmagnetic state, we introduce a magnetic moment and carry out two normal self-consistency iterations. This allows the potential to adjust to match the magnetic moment, but it will lower the (unstable) moment itself. The moment is then reset back to the starting value and another two cycles are run. This process is repeated until the potential stops changing. What we are left with in the end is a *fully self-consistent electronic structure with a locked magnetic moment*.

Recall that the driving force for ferromagnetism was the removal of M-M antibonding states from the vicinity of ε_F as a result of the exchange splitting. The exchange splitting itself—as well as the differing spatial extents of the two spin sublattices—arises because of differential shielding of the α and β electrons. In other words, the exchange splitting provides a measure of the extent of differential shielding. Plots of the calculated exchange splitting versus the spin-locked magnetic moment for Ni, Pd, and Pt in the range $0.0\,\mu_B \le \mu \le 0.5\,\mu_B$ (not shown here) are essentially linear. Least-squares fits to the data give slopes of 0.66, 0.47, and 0.45 eV$\,\mu_B^{-1}$ for Ni, Pd, and Pt, respectively; the exchange splitting in Ni increases much more quickly with increasing magnetic moment than that in Pd. Clearly, Pt is very similar to Pd and, at least in terms of the exchange splittings, Ni responds more dramatically to the presence of a magnetic moment.

Another difference between Ni and Pd can be seen by examining the spin-polarized M-M COHP curves from the spin-locked calculation with $\mu \equiv 0.5\,\mu_B$, shown in Figure 24. The difference in magnitude of the Ni α and β COHP curves, as well as the exchange splitting between the two spin sublattices, is clearly visible. For Pd, on the other hand, the α and β COHP curves are very similar in size and the exchange splitting is quite small. The spin-locked magnetic moment does force the α and β sublattices apart in energy. However, this shift is small and there is little or no change in the spatial extents of the spins.

In Figure 25 is another difference between transition series: the changes in the M-M ICOHP values as the spin-locked moment increases. Here we see that the Ni-Ni ICOHP decreases considerably faster (and the bond strength goes up more quickly) than those in Pd or Pt, which are again similar to each other. Although the M-M bonds strengthen in all three metals with increasing magnetic moment, the ICOHP for Ni increases more rapidly. Once again, Ni seems to be perturbed more by the presence of a magnetic moment than either Pd or Pt.

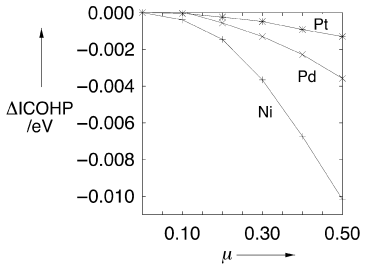

Figure 25. Changes in M-M ICOHP values with increasing spin-locked magnetic moment for Ni, Pd, and Pt.

For the second and third row transition metals, the presence of a magnetic moment does not alter the bonding significantly. Thus, although the antibonding states at ε_F may "push" towards a ferromagnetic structure, its formation does not result in a large enough exchange splitting to remove those states and the metals remain nonmagnetic.

The differences between Ni and Pd or Pt may be understood in the same way as we explained the differences between O_2 and S_2 or Se_2. The first-row transition metals have a special set of orbitals: the 3d orbitals. These are not shielded by any symmetry-similar orbitals in the core and are thus fairly contracted. Small changes to the shielding of the 3d orbitals, caused by spin polarization, give rise to comparably large changes in their energies and spatial extents. On the other hand, Pd and Pt have d functions in the core which help to screen their valence d orbitals. The small perturbations

from spin polarization do not have such a dramatic effect upon these well shielded orbitals. Consequently, the higher transition metals will not become ferromagnetic.

Here is a chemical analogy: We have seen that the special behavior of the light main-group elements, such as carbon, nitrogen, and oxygen, with respect to both magnetism and their "chemistry" can be traced back to the "missing" 1p orbital. Because of that, the susceptibility of these atoms to spin polarization is significantly enhanced. In these elements the 2s and 2p orbitals have similar spatial requirements. This has well known consequences for element–element multiple bonding, organic chemistry, and all the rest.

The situation for iron (and cobalt and nickel) is somewhat similar. Because of the "missing" 2d orbital, spin polarization does lead to large exchange splittings and a strengthening of metal–metal bonding (easily seen in the COHP curves). In this respect, the exceptional finding of ferromagnetism within the transition metals may be looked upon as analogue of the special situation of carbon chemistry within chemistry as a whole.

4.8. Ferromagnetism and Chemical Hardness

Using the standard definition of the term [Eq. (9)], the chemical hardness η of a metal is always zero because it has no gap between occupied and unoccupied levels.[30] However, hardness can be determined more rigorously from the first derivative of the chemical potential with respect to the number of electrons N. Since the chemical potential in metals is identical with the Fermi energy, we can express the chemical hardness of a conductor as Equation (11), where N_0 is the number of valence electrons in the neutral system and the subscript V indicates that the derivative is being taken with a frozen potential.

$$\eta = \frac{1}{2}\left(\frac{\partial \varepsilon_F}{\partial N}\right)_{V,N_0} \tag{11}$$

Equation (11) allows us to simply determine the chemical hardness of a transition metal from the slope of a plot of $\varepsilon_F(N)$ versus N at $N = N_0$.[41] Such a plot is shown for both the nonmagnetic and magnetic "forms" of α-Fe in Figure 26. It is clear that ε_F depends more or less linearly on N in the region around N_0 ($N_0 = 8$ for α-Fe) and that the slope of the curve *increases* with the onset of magnetism. A linear least-squares fit of the points between 7.9 and 8.1 valence electrons gives η values (half the calculated slope) of 0.132 eV and 0.428 eV for nonmagnetic and magnetic α-Fe, respectively. The chemical hardness of iron more than triples upon spin-polarization! Analogous increases in η are observed for Co (0.198 → 0.384 eV) and Ni (0.115 → 0.235 eV). In contrast to these drastic results, the η values of Pd in its nonmagnetic (0.202 eV) and spin-locked ($\mu \equiv 0.5\,\mu_B$; 0.256 eV) "forms" are not too different. Compared with the 0.115 → 0.220 eV hardness change for spin-locked Ni ($\mu \equiv 0.5\,\mu_B$), the value of η changes very little when Pd is forced to be magnetic.

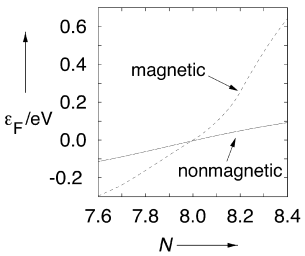

Figure 26. Calculated ε_F versus N curves for nonmagnetic (solid line) and magnetic (dashed line) α-Fe in the vicinity of N_0 (N_0, the number of valence electrons, is 8.0 in Fe). Both curves have been shifted so that $\varepsilon_F(N_0) = 0.0$ eV.

To further explore the connection between chemical hardness and magnetism, the hardnesses of all of the transition metals were calculated (Table 2). These hardnesses, based upon nonmagnetic calculations, reveal a curious fact: The *only* metals with hardness values below 0.2 eV are those that are ferromagnetic! In addition to this, *all* of the ferromagnetic metals have $\eta < 0.2$ eV! In other words, for all transition metals a necessary and sufficient condition for ferromagnetism is Equation (12)

Table 2. Calculated chemical hardness values [eV] for the elemental metals of all three transition series. The results were derived from least-square fits of $\varepsilon_F(N)$ plots calculated for the nonmagnetic "forms". Mn was calculated in the hypothetical bcc structure, discussed above.

M	η	M	η	M	η	M	η
Sc	0.280	Ti	0.528	V	0.282	Cr	0.723
"Mn"	0.165	Fe	0.132	Co	0.198	Ni	0.115
Y	0.481	Zr	0.509	Nb	0.368	Mo	0.862
Tc	0.544	Ru	0.611	Rh	0.402	Pd	0.202
La	–	Hf	0.718	Ta	0.422	W	1.077
Re	0.698	Os	0.820	Ir	0.552	Pt	0.252

$$\eta < 0.2 \text{ eV} \tag{12}$$

The same relation holds for all of the ferromagnetic alloys we will discuss below ($FeNi_3$, Fe_3Pd, $FePd_3$, and MnSb) with the single exception of FePd. Though we are certain that there are other exceptions to this rule that lurk in the myriad of ferromagnetic (and nonmagnetic) alloys known, it is quite remarkable and surprising that such a simple rule is able to accurately describe and predict ferromagnetism in all of the transition metals (including borderline cases such as Co and Pd) and many ferromagnetic alloys.

At a qualitative level, we feel that it is fairly straightforward to understand this connection between chemical hardness and ferromagnetism by, again, falling back on the chemistry of atoms and molecules. An atom or molecule with a low chemical hardness tends to have a high polarizability, that is, it is easy to rearrange its electronic charge distribution. As we have shown in detail for α-Fe, a redistribution of charge density is required for the transition from the nonmagnetic to the magnetic state. These electron shifts are easier to realize in soft rather than in hard metals. The origin of the mysterious 0.2 eV quantity in Equation 12 is not yet clear and is still under investigation.

Within the definition of Equation 11, the chemical hardness of a metal is very sensitive to the value of the density of states at ε_F. At large values of DOS(ε_F), small changes to the number of electrons do not significantly affect the position of ε_F; the metal will be chemically soft. A plot (not shown) of η versus DOS(ε_F) can be fit very satisfactorily with the function $\eta = 6.53/\text{DOS}(\varepsilon_F)$. However, since the DOS at ε_F alone cannot account for ferromagnetism (see the earlier discussion about

the Stoner criterion in Section 2.3), there must be some other essential physical quantity carried within the chemical hardness concept. What that is remains unclear at this point.

5. Interlude: Modern Developments in the Physics Community

Although Stoner's arguments have dominated the reasoning of many physicists within the last five decades, there have been other, more modern ideas. Here we give a short overview of two of the more prominent directions of research.

5.1. The Hubbard Model and Its Relatives

The Hubbard model[42] for the electronic structure of solids with strong electron–electron interactions has been quite successful at explaining the anomalous behavior of Mott insulators.[43] In this simple, powerful, but mathematically awkward model, there is a one-electron (hopping) energy term H_{ij} competing, as a function of the band-width parameter W (ΔE_{BW} in Figure 11), with an electron-electron repulsion parameter U.

The Hubbard model has been widely applied to ferromagnetic systems with flat bands.[44, 45] Simply speaking, our qualitative treatment of rare-earth ferromagnetism in Figure 11 a was intuitively based on the assumption of a repulsion parameter U which is much larger than the small bandwidth W. The scenario in Figure 11 b corresponds to the opposite limit, producing an ordinary, half-filled metallic band. In order to understand itinerant-electron ferromagnetism (as observed in the transition metals) in more detail, extensions of Hubbard's model are required. A number of these extensions have also been pursued with varying degrees of success.[46, 47] In an exhaustive series of publications, the impact of adding various additional interactions to the Hubbard model has been studied by Hirsch and coworkers.[48–54] Applications of the Hubbard model to metallic ferromagnetism have been recently reviewed.[55]

The problem with applying many of these Hubbard or Hubbard-like models to the understanding of ferromagnetism in transition metals and their alloys is that they presume systems have either a single band or a set of degenerate bands. While these simplifications are made in order to make the models exactly solvable (or as close as possible), much of the fundamental physics is lost. The elemental transition metals do *not* have bands which are either flat or purely degenerate. We feel that it is preferable to use a model which, although not exact, contains at least the correct behavior of the metallic bands.

5.2. First-Principles Calculations

Building upon the foundations of the Thomas–Fermi model for the electronic structure of atoms,[56–59] Hohenberg and Kohn developed the fundamental underpinnings of density-functional theory (DFT) in 1964.[60] In the following year, Kohn and Sham provided a set of equations which allowed this new theory to actually be applied to determine the electronic structure of real systems; in addition they introduced the local density approximation (LDA).[61] Kohn and Sham also realized the intimate connection between their new theory and the Xα method developed earlier by Slater.[62] In 1972, von Barth and Hedin generalized both the density-functional theory itself and the local density approximation to systems with unpaired spins.[63]

Just as it did for the body of solid-state theory, DFT (particularly in its spin-polarized form) revolutionalized the study of ferromagnetism. Given the enormous quantity of literature in the area, we here provide only an overview and a few highlights. For a comprehensive overview of recent first-principles studies of ferromagnetism and antiferromagnetism, see ref. [64] and references therein.

In 1975, Vosko and Perdew proposed a Stoner-like model to be used to approximate the magnetic susceptibilities of metals based upon their ground-state properties.[65] This model was extended to transition metals by Gunnarsson by using a set of approximate wave functions.[66] In 1977, Andersen et al. presented a systematic study of the electronic structure of iron and a number of other transition metals, as well as an approximation that allowed the parameters of the Stoner model to be extracted from their results.[18] That same year a paper, arguably among the most influential in the field, was published by Janak.[19] Janak, working from the model presented by Vosko and Perdew,[65] extracted the Stoner parameters for all of the first- and second-row transition metals, as well as many simple metals (see Figure 2) from their electronic structures as calculated within spin-density functional theory. In 1978, Moruzzi, Janak, and Williams coauthored a book which compiled the electronic structures of the metals.[67]

Problems with the local spin-density approximation (LSDA) were discovered in 1981 by Kübler, who realized that, at least within the augmented spherical-wave (ASW) method, the calculated energy of antiferromagnetic face-centered cubic iron was lower than that of the ferromagnetic body-centered cubic phase.[68] Wang et al., using the linear-augmented plane-wave (LAPW) method, generalized this result and concluded that the LSDA did not predict the correct ground state for iron.[69] Four years later, Bagno et al. demonstrated that the introduction of gradient corrections to the LSDA removed these problems.[70]

In a series of papers published in the late 1980s and early 1990s, Moruzzi, Marcus, and co-workers produced a comprehensive study of the structural and magnetic properties of the 3d and 4d transition metals using a fixed spin-moment procedure within the ASW method. By holding the magnetic moment fixed and iterating until self-consistency was reached, Moruzzi et al. were able to study the potential-energy surfaces for both the onset of ferromagnetism in the first-row[71, 72] and some second-row[73] transition metals. The energetic circumstances of antiferromagnetism in both the 3d[74] and 4d[75] metals were also studied and discussed.

In this Review, we have essentially followed the density-functional theory route. Indeed, our findings are all based

upon the results of spin-density-functional calculations (see Appendix A). While density-functional theory does provide quantitative answers in many—but not all—cases, its advantage is, however, mostly due to it being an orbital theory, making a chemical interpretation easy. This is the goal of our approach, extending a theoretical track which originated within theoretical physics and making it compatible with related ideas of theoretical chemistry (see Appendices A.2 and B).

6. Ferromagnetism in Alloys

With reference to Section 4, we will now demonstrate that the same ideas developed to explain ferromagnetism in metallic elements can be applied also to metallic alloys.[76] Due to restrictions imposed by our computational methodology and resources, we limit our attention to ordered binary alloys; we are confident that this discussion applies to both disordered structures and alloys containing more than two elements.

6.1. A Model for Spin Polarization in Binary Systems

While Figure 12 provided the qualitative underpinnings necessary to interpret the densities of states of magnetic transition metals, it requires some modifications in order to understand those of alloys. The following model is intended to serve for a better understanding in more complicated systems; the impatient reader may go directly to the next Section, which offers realistic calculations without assumptions.

Consider the alloy $M_xM'_y$. Since M and M′ are different types of atoms, their projected densities of states will certainly have different sizes and bandwidths. These differences and their effects upon the spin-polarization process are sketched qualitatively in Figure 27. A number of assumptions and simplifications went into this. Listed in order of increasing severity they are:

- We are using a rigid-band model: The forms and compositions of the crystal orbitals do not change upon spin polarization (that is, the α- and β-DOS curves have exactly the same shape and size but occur just at different energies).
- The shifts in the energies of the α and β sublattices upon spin polarization (exchange splittings) are assumed to be the same in panes b) and d).
- The exchange splittings in the DOS of M and M′ are the same.

Despite this massive oversimplification of a truly complicated problem, the DOS curves in Figure 27b and 27d reveal several important findings about magnetism in alloys. Unlike the simple elemental transition metals, where each atom is identical, the different atom types in alloys do not necessarily carry the same local magnetic moments. For example, in Figure 27b, the difference between the occupations of the α and β sublattices of M—which determines the number of unpaired electrons on M—is four boxes, while that between

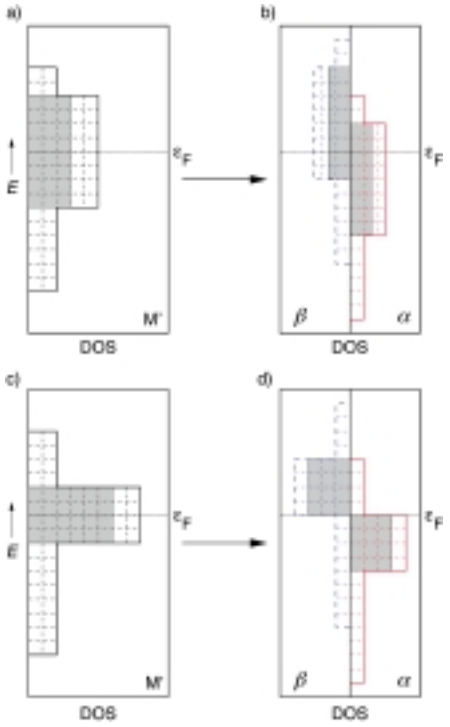

Figure 27. Qualitative DOS curves for a binary transition-metal alloy $M_xM'_y$. In a) and b) are the DOS and spin-polarized DOS of an alloy where the bandwidth of M′ is one-half that of M. In c) and d) are the DOS and spin-polarized DOS of an alloy where the bandwidth of M′ is one-quarter that of M. In all four panes, the horizontal dotted line indicates the position of the Fermi level (ε_F) and the shaded region corresponds to the M′ projected DOS. The dashed grid superimposed on the DOSs is included to facilitate the counting of states.

the α and β sublattices of M′ is six boxes. Thus M′ has a higher local magnetic moment than M.

In the second case, where the distribution of M′ states is half as broad and their contribution to the DOS around ε_F is larger (Figure 27d), the local moment on M is still determined by the four box difference, but all of the M′ α states are occupied while all of the M′ β states are empty. The local magnetic moment of M′, calculated from a differential occupation of twelve boxes, is thus twice as large as it was before. This observation may be generalized to give a rule of thumb for transition metal alloys: Those atoms with the largest contributions to the nonmagnetic DOS around ε_F will also have the largest local moments upon spin-polarization.

6.2. Alloys Between Ferromagnetic Metals: Realistic Calculations

Our archetype for a binary alloy between two ferromagnetic transition metals is $FeNi_3$. This alloy crystallizes in the $AuCu_3$ structure,[77] an fcc arrangement of nickel atoms in which every fourth Ni has been replaced by Fe in an ordered fashion (Figure 28). The lattice constant (3.552 Å) is only

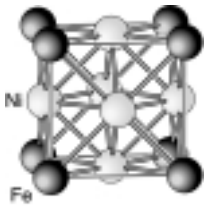

Figure 28. The unit cell of $FeNi_3$ with the $AuCu_3$ structure.

slightly larger than that of elemental Ni (3.524 Å). The experimental magnetic moment of $FeNi_3$ is 1.18 μ_B.[78] Neglecting the fact that $FeNi_3$ is a structurally ordered alloy, its valence-electron concentration (9.5 electrons per atom) allows us to think of it as either a heavily electron-enriched fcc Fe or a slightly electron-poor fcc Ni.

As we did with α-Fe, we start by examining the results of a nonmagnetic calculation of $FeNi_3$ (Figure 29). One might expect that $FeNi_3$ is electronically similar to elemental Ni and, indeed, its DOS is almost superimposable on that of Ni (Figure 21). The major difference is that ε_F is located in a sharp, narrow DOS peak at the top of the d block. The Fe

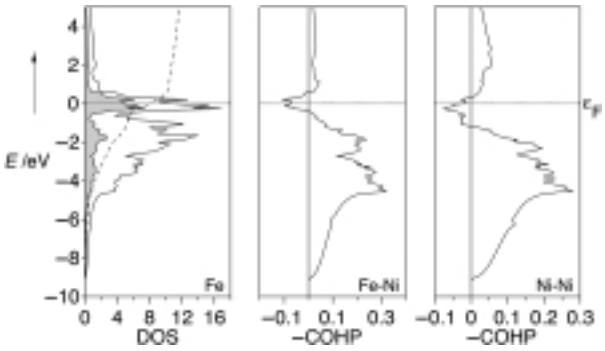

Figure 29. Calculated DOS, Fe-Ni, and Ni-Ni COHP curves for nonmagnetic $FeNi_3$. The shaded region and dashed line in the DOS curve corresponds to the projected DOS of the Fe atom and its integration, respectively. All curves have been shifted in energy so that ε_F, indicated with a horizontal dotted line, lies at 0.0 eV.

states (projected DOS in Figure 29) are spread almost evenly throughout the DOS except for the sharp peak at ε_F, which is almost half derived from Fe. Since only one quarter of the atoms are Fe, this is a quite large contribution. Given that Ni is more electronegative than Fe (the Pearson absolute electronegativities are 4.40 eV and 4.06 eV respectively),[30] we would have expected the upper regions of the d block to be mostly Fe. The chemical hardness of $FeNi_3$, corrected for the presence of four atoms in the unit cell, is 0.182 eV and lies comfortably below the proposed cutoff value for the appearance of ferromagnetism (0.2 eV).

We now turn to the COHP curves of Figure 29. The Fe-Ni and Ni-Ni COHP curves are very similarly shaped and have ICOHP values of -1.130 and -0.961 eV per bond, respectively. The sharp peak at the top of the d block is, as expected, strongly antibonding for both Fe–Ni and Ni–Ni bonds. As in the elements, these strongly antibonding states at ε_F give rise to an instability with respect to a ferromagnetic distortion in $FeNi_3$.

A spin-polarized calculation of its electronic structure results in an average spin moment of 1.182 μ_B, in quantitative agreement with the experimental data. The DOS and COHP curves for magnetic $FeNi_3$ are presented in Figure 30. In addition to being shifted in energy, the α and β DOS curves are also quite differently shaped. The α DOS is almost uniform in shape—very similar to that in magnetic Ni (Figure 20)—while the β DOS retains a sharp peak at the top of the d block. Although the Fe states are spread

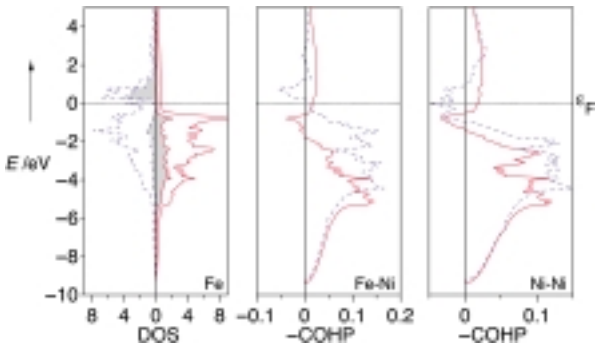

Figure 30. Calculated DOS, Fe-Ni, and Ni-Ni COHP curves for magnetic $FeNi_3$. The shaded region in the DOS curve corresponds to the projected DOS of the Fe atom. In each plot, the solid red/dashed blue line corresponds to the α/β spins. All curves have been shifted in energy so that ε_F, indicated with a horizontal dotted line, lies at 0.0 eV.

essentially evenly throughout the d block in the α DOS, they remain a major contributor to the sharp peak above ε_F in the β spin sublattice.

Based upon the qualitative picture for the magnetic moments in alloys presented above, we would expect Fe (which makes a large contribution to a set of narrow states at ε_F in the nonmagnetic electronic structure) to have a high local magnetic moment in $FeNi_3$. This is shown in the calculated local magnetic moments: 2.878 μ_B for Fe and 0.617 μ_B for Ni. As we shall see, the high moment for Fe (as compared to that in metallic iron) is typical in alloys between Fe and other late transition metals. The Ni moment is very similar to that calculated for elemental Ni. The chemical hardness of magnetic $FeNi_3$ is 0.546 eV, three times larger than in the nonmagnetic calculation.

Based upon the differences in the calculated net charges in the magnetic and nonmagnetic systems,[79] each Fe transfers approximately 0.09 electrons to the Ni atoms upon spin polarization. This charge transfer, which is not included in the simple model of Figure 27, is in large part due to the fact that the exchange splitting of the Fe states in $FeNi_3$ is larger than that of the Ni states.

The Fe-Ni and Ni-Ni COHP curves of Figure 30 are analogous to those in the preceding sections: In both sets of COHP curves, the β spin sublattice has stronger interactions than α and the antibonding character of the states at ε_F has been either reduced or removed completely (see Fe-Ni COHP curves). In magnetic $FeNi_3$, the Fe-Ni and Ni-Ni ICOHPs are -1.114 and -1.105 eV per bond, respectively; spin polarization has weakened the covalent part of the Fe–Ni bonds by 1.4 % and strengthened the Ni–Ni bonds by more than 15 %. Interestingly enough, the Ni–Ni bonds in magnetic $FeNi_3$ are even stronger than those in magnetic Ni (ICOHP = -0.996 eV per bond), which may hint towards the driving force to adopt an ordered atomic arrangement. Since there are more Ni–Ni than Fe–Ni bonds, the net result of these changes is an increase in bonding.

Despite the extra complications arising from the presence of two different sorts of atoms in the unit cell, the qualitative features of ferromagnetism in $FeNi_3$ are similar to those seen in the elemental transition metals; refer to points 1 – 4 in the discussion of Co and Ni in Section 4.4.

6.3. Alloys Containing a Single Ferromagnetic Metal

Let us now replace one of the ferromagnetic elements with a nonferromagnetic one but remain with a ferromagnetic alloy. One "natural" choice is the iron/palladium system, where alloys are known with average valence electron concentrations of 8.5 (Fe_3Pd), 9.0 (FePd), and 9.5 ($FePd_3$) electrons per metal atom. Fortunately, all of these phases adopt fcc-like structures, with Fe_3Pd[80] and $FePd_3$[81] crystallizing in the $AuCu_3$ structure type (Figure 28) and FePd[82] in the AuCu structure type (Figure 31). Conflicting claims of substitutional disorder further complicate the structural chemistry of these alloys.

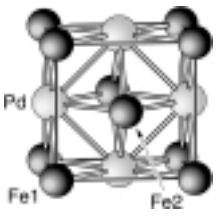

Figure 31. The structural motif of FePd with the AuCu structure.

For the sake of brevity, we will discuss the electronic structures of the alloys together. The DOS and COHP curves for both the nonmagnetic and magnetic calculations of Fe_3Pd, FePd, and $FePd_3$ are presented in Figures 32–37. Numerical details of the interatomic bond strengths (as measured by ICOHP values), calculated magnetic moments and chemical hardnesses are presented in Table 3.

To start with, all three alloys have antibonding Fe-Pd as well as Fe-Fe and/or Pd-Pd interactions at ε_F in their unstable

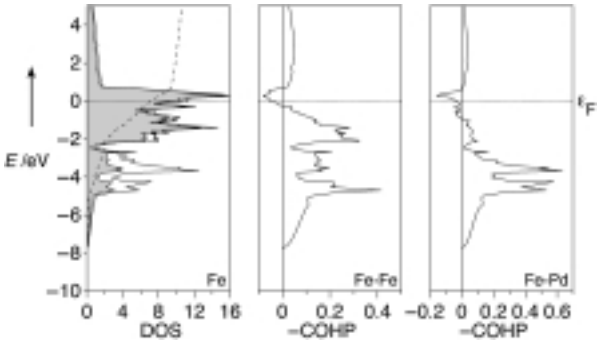

Figure 32. Calculated DOS, Fe-Fe, and Fe-Pd COHP curves for nonmagnetic Fe_3Pd. The shaded region and dashed line in the DOS curve corresponds to the projected DOS of the Fe atom and its integration respectively. All curves have been shifted in energy so that ε_F, indicated with a horizontal dotted line, lies at 0.0 eV.

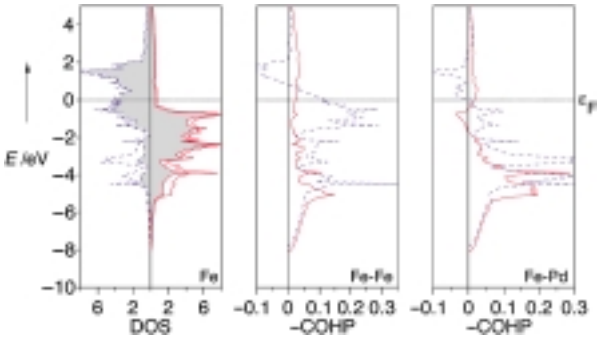

Figure 33. Calculated DOS, Fe-Fe, and Fe-Pd COHP curves for magnetic Fe_3Pd. The shaded region in the DOS curve corresponds to the projected DOS of the Fe atom. In each plot, the solid red/dashed blue line corresponds to the α/β spins. All curves have been shifted in energy so that ε_F, indicated with a horizontal dotted line, lies at 0.0 eV.

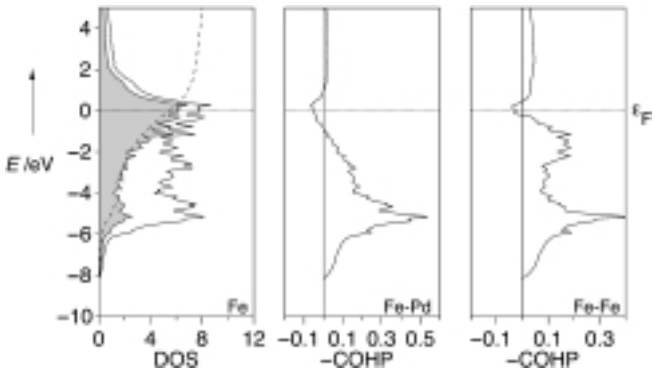

Figure 34. Calculated DOS, Fe-Pd, and Fe-Fe COHP curves for nonmagnetic FePd. The shaded region and dashed line in the DOS curve corresponds to the projected DOS of the Fe atom and its integration respectively. All curves have been shifted in energy so that ε_F, indicated with a horizontal dotted line, lies at 0.0 eV.

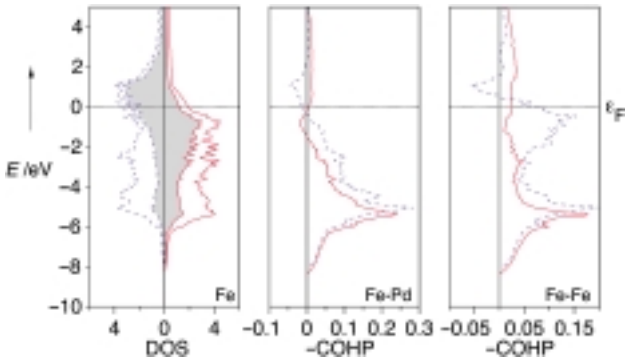

Figure 35. Calculated DOS, Fe-Pd, and Fe-Fe COHP curves for magnetic FePd. The shaded region in the DOS curve corresponds to the projected DOS of the Fe atom. In each plot, the solid red/dashed blue line corresponds to the α/β spins. All curves have been shifted in energy so that ε_F, indicated with a horizontal dotted line, lies at 0.0 eV.

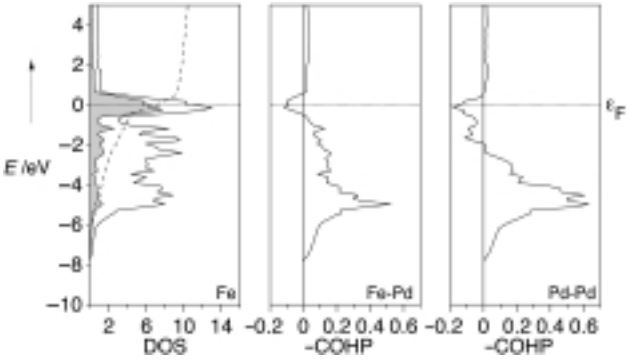

Figure 36. Calculated DOS, Fe-Pd, and Pd-Pd COHP curves for nonmagnetic $FePd_3$. The shaded region and dashed line in the DOS curve corresponds to the projected DOS of the Fe atom and its integration respectively. All curves have been shifted in energy so that ε_F, indicated with a horizontal dotted line, lies at 0.0 eV.

nonmagnetic "forms" (Figures 32, 34, 36). This is most easily seen for the more electron-rich alloys (FePd and $FePd_3$) but is seen also for Fe_3Pd. A prediction of ferromagnetism would thus be justified for all three. This prediction is borne out by the results of the spin-polarized calculations (Table 3), which, for Fe_3Pd and $FePd_3$, match satisfactorily with the few pieces

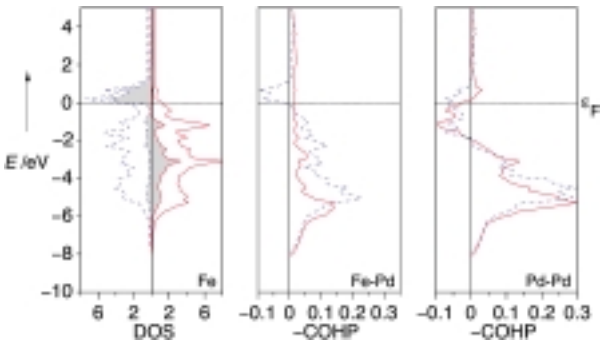

Figure 37. Calculated DOS, Fe-Pd, and Pd-Pd COHP curves for magnetic $FePd_3$. The shaded region in the DOS curve corresponds to the projected DOS of the Fe atom. In each plot, the solid red/dashed blue line corresponds to the α/β spins. All curves have been shifted in energy so that ε_F, indicated with a horizontal dotted line, lies at 0.0 eV.

of experimental data available[33, 83] and independent first-principles calculations.[84, 85] For FePd, our calculations seem to somewhat underestimate the sizes of the individual moments. Nevertheless, there is general agreement that all three alloys are ferromagnetic with approximate moments of 0.3 μ_B for Pd and 2.6 μ_B for Fe; the latter moment is known to rise beyond 3 μ_B with increasing Pd concentration, in good agreement with neutron diffraction data.[86] We believe more experimental studies, with respect to structure, composition, and order, might be needed for this binary system.

Upon spin polarization, the total energies of Fe_3Pd, FePd, and $FePd_3$ lower by 1.35, 0.32, and 1.21 eV, respectively. This is paralleled by increases in the overall bonding strengths of 6.3, 1.1, and 1.7 % (calculated by summation of all ICOHP values in the unit cell). With the exception of a single set of interactions (the Fe-Pd bonds in $FePd_3$), all bonds in these alloys are strengthened by the shifting of antibonding states away from ε_F. The loss of Fe-Pd bonding energy in $FePd_3$ is more than counterbalanced by the increase in Pd-Pd bonding. As expected from the calculations on the pure elements discussed above, the exchange splitting for the Fe states is much larger than that for the Pd states. This large difference in exchange splitting, along with the Fe domination of the states at ε_F in all three alloys, leads to the considerably higher (roughly an order of magnitude) magnetic moments of Fe.

It is interesting to note that some spin-polarized COHP curves no longer exhibit antibonding contributions in the α spin sublattice (majority); this can been seen for the Fe-Fe bonds of Fe_3Pd (Figure 33) and FePd (Figure 35) as well as the Fe-Pd bonds of $FePd_3$ (Figure 37). This curious phenomenon can be understood by considering the M-M distances in these structures.

In Fe_3Pd and FePd, the Fe–Fe distances (2.70 and 2.73 Å, respectively) are considerably longer than those in α-Fe (2.48 Å), a result caused by the spatial requirements of the large Pd atoms. For the Fe 3d orbitals in the highly contracted α spin sublattice, these distances are effectively larger still. The Cu-Cu COHP curve in Figure 21 demonstrates that, in systems with highly contracted d orbitals, the bonding arising within the s band (which penetrates the entire d block) outweighs the antibonding contributions from the d states at the top of the d block. The result in Cu is a COHP curve which is, in the energy window we examine, almost completely bonding throughout. The Fe-Fe bonds in Fe_3Pd and FePd show the same effects: the Fe 4s states are not significantly perturbed by the spin polarization, and the 3d contributions to the α DOS are highly contracted. The Fe–Pd bonds in $FePd_3$ (2.72 Å) are not much longer than those in Fe_3Pd (2.70 Å) or FePd (2.68 Å), yet the same phenomenon is observed because of the very high local magnetic moments on the Fe atom (3.333 μ_B). The α 3d states on Fe here are even more contracted than those in Fe_3Pd and FePd.

With the exception of FePd, the chemical hardness values of these alloys also fit our expectations: The η values, which start from less than 0.2 eV in the nonmagnetic "phases", increase dramatically with the onset of magnetism. The FePd alloy is an exception (and the only one we have found at this point) to our rule that the calculated η of the nonmagnetic "form" of a ferromagnetic substance should be less than 0.2 eV. Upon spin polarization, the hardness of FePd does increase, as expected. Further exploration of this area is necessary.

With a few exceptions, the qualitative characteristics of ferromagnetism in these ordered Fe-Pd alloys follow the rules developed above for both the pure transition metals and $FeNi_3$.

6.4. Alloys without Ferromagnetic Metals

Since the early days of metallurgical research on ferromagnets, experimentalists have produced, mostly by trial-and-error synthetic strategies, an astounding variety of ferromagnetic alloys which do not contain any ferromagnetic metals (that is, alloys without Fe, Co, or Ni). Among these phases the Heusler alloys X_2YZ (for example, Cu_2MnAl, which has a Curie temperature of around 600 K[87]) are probably the most prominent. In the Heusler alloys, the Y atoms form a face-centered cubic lattice while the X and Z atoms occupy all of the tetrahedral and octahedral voids, respectively.[88]

Here we will examine an even simpler, possibly more fundamental case: MnSb. This material, which has a Curie

Table 3. Calculated values for the Fe/Pd alloys.

	ICOHP [eV]						η [eV]		Local magnetic moments [μ_B]	
	nonmagnetic			magnetic			nonmagnetic	magnetic	μ(Fe)	μ(Pd)
	Fe-Pd	Fe-Fe	Pd-Pd	Fe-Pd	Fe-Fe	Pd-Pd				
Fe_3Pd	– 0.925	– 0.980	–[a]	– 0.981	– 1.043	–[a]	0.184	0.392	2.760	0.294
FePd	– 1.078	– 0.949	– 0.944	– 1.086	– 0.949	– 0.969	0.258	0.408	2.257	0.170
$FePd_3$	– 0.957	–[a]	– 0.994	– 0.937	–[a]	– 1.023	0.196	0.416	3.333	0.342

[a] Not calculated.

temperature of 600 K,[89] adopts the NiAs structure type (Figure 38). In this structure, the Mn atoms are octahedrally coordinated by Sb and the Sb atoms are found in a trigonal prism of Mn. The Mn–Sb distance is 2.805 Å. The Mn atoms

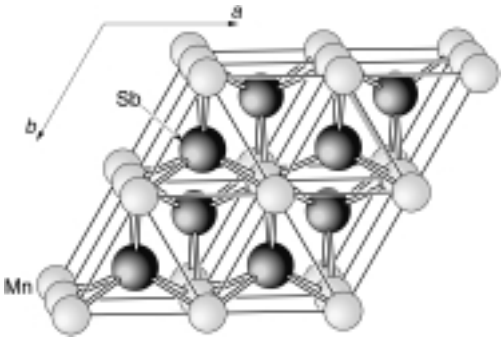

Figure 38. A view along the *c* axis of the structure of MnSb (NiAs structure type).

form linear chains with Mn–Mn distances of 2.878 Å.[90] The experimental bulk magnetic moment of $Mn_{1.09}Sb$ is 3.25 μ_B. Polarized-neutron diffraction experiments reveal a local (Mn-centered) moment of 3.45 μ_B.[91] The difference between these two numbers indicates that each Sb atom carries a moment of about 0.20 μ_B oriented in the *opposite* direction from that on Mn. Strictly speaking, MnSb is thus better described as a *ferrimagnetic* alloy. Our electronic interpretation does not have to be modified in order to cover this additional perturbation though.

The electronic structure of nonmagnetic MnSb is shown in Figure 39. Though the DOS peak, which runs from -5 to 3 eV and contains the Fermi level, is composed of both Mn 3d and Sb 5p states, the region directly around ε_F itself is heavily

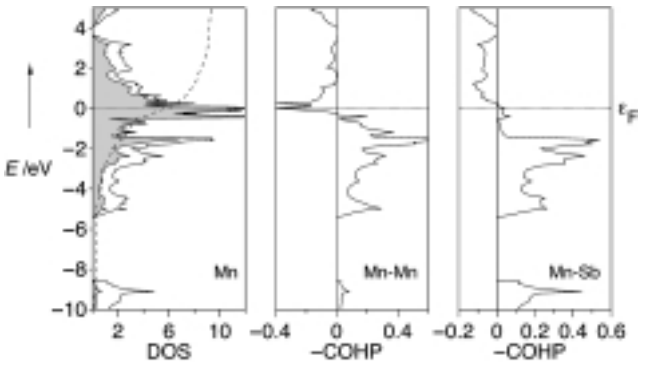

Figure 39. Calculated DOS, Mn-Mn, and Mn-Sb COHP curves for nonmagnetic MnSb. The shaded region and dashed line in the DOS curve corresponds to the projected DOS of the Mn atom and its integration respectively. All curves have been shifted in energy so that ε_F, indicated with a horizontal dotted line, lies at 0.0 eV.

dominated by Mn. The states arising from the Sb 5s orbitals are partially visible at the bottom of the DOS curve. Because the Mn 3d and Sb 5p orbitals are close to each other in energy and because of the strength of the Mn-Mn interactions, the expected e_g-t_{2g} splitting of the Mn 3d states is not visible here. All of the occupied states are in the Mn-Sb bonding region, whereas ε_F falls in a strongly Mn-Mn antibonding region. The calculated Mn-Sb and Mn-Mn ICOHP values are -1.349 and -1.081 eV per bond, respectively. The absolute electronegativities of Mn (3.72 eV) and Sb (4.85 eV)[30] lead us to suspect that Sb should be the "anionic" component in this intermetallic alloy.

The presence of ε_F in antibonding states indicates that MnSb would prefer to adopt a ferromagnetic structure. In addition, the large Mn contributions to the DOS near ε_F should point to a large local magnetic moment on Mn in the magnetic phase. A spin-polarized calculation of the electronic structure of MnSb gives a magnetic moment of 3.24 μ_B. This moment is formed from the 3.37 μ_B (Mn) and -0.13 μ_B (Sb) local magnetic moments. These results are in satisfying agreement with the experimental values given above, and the small differences easily attributable to the fact that the experimental measurements were carried out on a nonstoichiometric (Mn-rich) compound. We can understand the small size of the local magnetic moment on Sb by realizing that Sb has no magnetically active orbitals; the Sb 4d orbitals are completely occupied and are of low energy and the valence 5s and 5p orbitals are very well shielded from the nucleus and do not have significant exchange splittings. As mentioned above, the large moment on Mn comes about because of the large contribution of Mn to the states near ε_F in the nonmagnetic electronic structure (Figure 39).

The DOS and COHP curves of the magnetic "form" of MnSb are shown in Figure 40. The Sb contributions to the total α and β DOS curves (the unshaded regions in Figure 40)

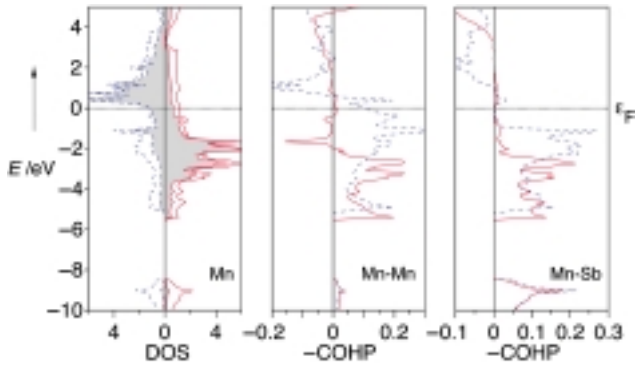

Figure 40. Calculated DOS, Mn-Mn, and Mn-Sb COHP curves for magnetic MnSb. The shaded region in the DOS curve corresponds to the projected DOS of the Mn atom. In each plot, the solid red/dashed blue line corresponds to the α/β spins. All curves have been shifted in energy so that ε_F, indicated with a horizontal dotted line, lies at 0.0 eV.

are very similar, as we would expect given that Sb states should not exhibit a large degree of exchange splitting. The spin-polarized DOS of MnSb is qualitatively composed of a nonmagnetic background arising from the Sb states with the magnetic Mn DOS superimposed. This is a useful way of thinking of MnSb itself: ferromagnetic chains of Mn atoms surrounded by an almost nonmagnetic sea of Sb atoms.

The calculated ICOHP values for the Mn–Sb and Mn–Mn bonds in ferromagnetic MnSb are -1.273 and -1.100 eV per bond, respectively. While the Mn–Mn bonds strengthen, as we would expect, the Mn–Sb bonds become considerably *weaker* upon spin polarization. This leads us to a very important

point: Although the presence of antibonding levels at ε_F in a nonmagnetic calculation indicates the presence of a driving force for spin polarization (which removes those levels from around ε_F), this does not necessarily mean that the total bond strength in the system must increase when it becomes magnetic. In other words, the antibonding character of the states around ε_F provides the *motivation* for ferromagnetism, but the "payback" does not necessarily have to come from a strengthening of bonds, as measured by ICOHP values. A closer analysis shows that the stabilization in MnSb results from atom-centered contributions (otherwise known as on-site COHP terms).[92]

The potential for ferromagnetism in MnSb may also have been predicted by the knowledge of the chemical hardness of its nonmagnetic "phase": 0.142 eV. With the emergence of ferromagnetism, η increases by more than a factor of 5 (!) to 0.766 eV, the largest increase we have found so far.

7. Epilogue and Future Perspectives

We have already come a long way in our exploration of the orbital origins of magnetism. As we have tried to explain, there are strong similarities in the changes wrought by magnetism as we increase in complexity from atoms to molecules to ferromagnetic alloys. Examination of the nature of the bonding (where appropriate) and the consequences of the exchange hole in all of these systems has led us to an understanding of a fascinating macroscopic quantum effect: ferromagnetism. According to our interpretation, ferromagnetism is a *chemical* phenomenon, arising only in systems with a critical electron concentration—one which causes ε_F to fall in a region of antibonding states. The resulting instability results in the expected lowering in symmetry. However, rather than altering the spatial coordinates of the atoms, the electronic symmetry is lowered by making the α and β spins inequivalent. This break in the electronic symmetry leads to energy level shifts, repopulation of the spin sublattices, and a redistribution of charge density. It is straightforward to extend this new interpretation of the phenomenon of ferromagnetism to complicated species such as alloys. The interpretation itself fits nicely into general useful chemical ideas such as the principle of chemical hardness.

7.1. Theory

The perceptive reader might have noticed that we have refrained from going too deeply into the curiosities of the localized-electron magnetism of the rare-earth metals. As we have tried to suggest, a chemical-bonding interpretation of magnetism arising from 4f orbitals seems to be ill fitting. Some preliminary calculations, however, indicate that similar thinking might be applied even here, at least for mixed d block/f block magnetic materials, such as $SmCo_5$ or $Nd_2Fe_{14}B$, where the spin–spin interactions are mediated through the conduction electrons (Rudermann-Kittel-Kasuya-Yoshida (RKKY)).[93–95]

With respect to numerical investigations, one of us (R.D.) is most curious to learn more about the almost coincidental decay of both the molecular field and the bond strength as a function of the interatomic distance. As it stands now, the other of us (G.A.L.) believes that it is purely accidental. The source of the mysterious size of the hardness criterion for ferromagnetism (0.2 eV) also needs to be studied. The latter project, however, would have to be based upon an analytical approach. Given the limited success of various model techniques to date (Hubbard model, and so forth) this goal might be challenging to achieve.

An extension of the interpretative COHP technique presented here to deal with *disordered* alloys is needed. A lot can be learned from the successes of various mean-field approaches, such as the coherent-potential approximation (CPA), a standard approach in theoretical solid-state physics.[96–99]

Work is also currently underway to understand the connection between antiferromagnetism and COHP curves. In particular, the importance of, and the role played by, the nonbonding states around ε_F for Cr is being studied.[100]

7.2. Syntheses and Experiments

Here is a recipe for the restless synthetic chemist trying to create new ferromagnetic materials: Try to adjust, by chemical means such as oxidation and reduction, the Fermi energy of the starting material in order to maximize the antibonding interactions between those atoms which have narrow band widths in their elemental forms. We have, in part, demonstrated the impact of such gradual electron fillings for the Fe_xPd_y alloys upon local atomic magnetic moments. One alternative example, of the hundreds or thousands which are also worth investigating, is given by the MnSb phase. Based upon the two nonmagnetic COHP curves, one might now envision the partial replacement of Mn or Sb by other metals, or even the introduction of oxidizing or reducing atomic species. Without our present knowledge about the structure of the COHP curves at ε_F, metallurgists long ago pursued this course by synthesizing ferromagnetic materials such as Cu_2MnSb. It remains to be seen what can be done when one follows a slightly more rational approach.

Due to the fact that the "alarm" signaling a preference for the ferromagnetic state (antibonding COHP(ε_F)) shows up in *nonmagnetic* band structure calculations, a properly parameterized semi-empirical (extended-Hückel tight-binding,[101–103] for example) calculation—nowadays so ubiquitous in solid-state chemical laboratories—can provide an equivalent COOP result to guide the experimentalist. This is discussed in somewhat more detail in Appendix B.

As a final synthetic challenge, we would like to suggest an attempt to prepare body-centered cubic manganese under standard conditions, having predicted that it will be a ferromagnet with a moment of about one Bohr magneton. Since the phase cannot be quenched from high temperature, a softer (perhaps organometallic) route may be required.

Appendix A: Computational Methodology

A.1. Solids

Electronic structure calculations on solids were performed using the linear muffin-tin orbital (LMTO) method[104–107] within the local spin-density approximation (LSDA)[63]. All calculations were checked for convergence of energies, orbital moments, integrated COHP values, and magnetic moments with respect to the number of k points used in the reciprocal space integrations.[108] Atomic sphere radii used in the TB-LMTO-ASA calculations were chosen using an automated procedure (TB = tight binding; ASA = atomic sphere approximation). The program used was TB-LMTO 4.7.[109]

While the LSDA is known to have problems with metallic Fe—predicting an antiferromagnetic fcc structure to be more stable than the magnetic bcc form[69] (see Section 5.2)—it reproduces the experimental magnetic moments of Fe, Co, and Ni (2.21, 1.74, and 0.62 μ_B per atom, respectively[33]) quite closely (2.27, 1.62, and 0.62 μ_B). The spin-polarized DOS of magnetic bcc Fe, generated using a gradient correction scheme within the framework of a linear augmented plane wave (LAPW) calculation,[110, 111] is essentially identical to that generated using the LSDA within the LMTO method. Since we are not interested here in energy differences between particular structures (using instead experimental structures and lattice constants), we believe that the LSDA is accurate enough for our purposes.

A.2. Crystal-Orbital Hamilton Population Analysis

Crystal-orbital Hamilton population (COHP) analysis[92] is a partitioning of the band structure energy (sum of the energies of the Kohn–Sham orbitals) in terms of orbital-pair contributions. The COHP analysis, while in many ways analogous to the familiar crystal-orbital overlap population (COOP) analysis used in extended Hückel calculations,[112, 113] provides a quantitative measure of bond strengths and is probably more appropriate for a first-principles calculation.

Before proceeding, a word about the connection between COHP and total energy is needed. Within the framework of density-functional theory, the total electronic energy $E_{tot}[\rho]$ is given in [Eq. (13)], where ρ is the electron density and $E_{kin}[\rho]$, $E_{Hartree}[\rho]$, $E_{el-nuc}[\rho]$, and $E_{xc}[\rho]$ are the kinetic, electron–electron repulsion, electron–nuclear attraction, and exchange–correlation energies.[31]

$$E_{tot}[\rho] = E_{kin}[\rho] + E_{Hartree}[\rho] + E_{el-nuc}[\rho] + E_{xc}[\rho] \quad (13)$$

By definition, the sum of all the integrated COHP values (the ICOHP value) in a system is equal to the band-structure energy, which is the sum of the Kohn–Sham one-electron eigenvalues,[92] [Eq. (14)], where the ICOHP sum includes both on-site (diagonal) and off-site (off-diagonal) terms, ε_i is the energy of the i-th Kohn–Sham orbital, and the subscripts j and k label atomic orbitals. The sum over eigenvalues in Equation (14) can be expanded to give Equation (15), where $\mu_{xc}(\vec{r})$ is the exchange–correlation potential.[31]

$$\sum_j \sum_k \int_{-\infty}^{\varepsilon_F} dE\, COHP_{jk}(E) = \sum_j \sum_k ICOHP_{jk} = \sum_i \varepsilon_i \quad (14)$$

$$\sum_j \sum_k ICOHP_{jk} = \sum_i \varepsilon_i = E_{kin}[\rho] + 2E_{Hartree}[\rho] + E_{el-nuc}[\rho] + \int d\vec{r}\, \mu_{xc}(\vec{r})\rho(\vec{r}) \quad (15)$$

Finally, substituting Equation (13) into Equation (15) gives us the connection between $E_{tot}[\rho]$ and the ICOHP values [Eq. (16)].

$$E_{tot}[\rho] = \sum_j \sum_k ICOHP_{jk} - E_{Hartree}[\rho] + E_{xc}[\rho] - \int d\vec{r}\, \mu_{xc}(\vec{r})\rho(\vec{r}) \quad (16)$$

Equations (15) and (16) demonstrate that 1) the ICOHP values contain contributions from all terms of the density-functional electronic energy and 2) there is a direct link between the ICOHP values and the total electronic energy of a system. The success of one-electron theories in quantum chemistry (for example, extended Hückel theory) is due in no small part to the intimate connection between the sum of one-electron eigenvalues (COHP terms) and the total energy. This connection is one of the pillars of qualitative molecular-orbital theory.

All COHP curves are presented here in a format similar to COOP curves: positive values are bonding and the negative antibonding (that is, we plot $-$COHP instead of COHP).

A.3. Molecular Orbital Calculations

Molecular-orbital calculations were carried out within the framework of density-functional theory using the Amsterdam Density Functional (ADF) program, version 2.3.[114–116] Triple-ζ Slater-type orbital (STO) basis sets with either one (Se) or two (O, S) polarization functions (ADF basis set V) were used to represent the valence orbitals; the core orbitals were frozen to 1s (O), 2p (S), and 3p (Se).[117] The local spin-density approximation (within the Vosko, Wilk, and Nusair parameterization[118]) was augmented using the Becke–Lee–Yang–Parr (BLYP) gradient correction scheme.[119, 120] All plots were generated using Viewkel, a part of YAeHMOP.[121]

Appendix B: The Extended Hückel Method and Magnetism

The extended Hückel theory[122–124] is known for its flexibility and the ease with which its results lend themselves to chemical interpretation. To those familiar with the method, it will come as little surprise that the qualitative features of the crystal-orbital overlap population (COOP) curves from a well parameterized, extended Hückel, tight-binding calculation[101–103] are qualitatively similar to the COHP curves from an equivalent calculation from a better method.[125] To demonstrate this, the extended Hückel band structure, DOS, and COOP curves for α-Fe are shown in Figure 41. Comparing these results with Figure 14, we see both similarities and differences. It is obvious that the parameterization chosen leads to an underestimation of s dispersion and an overestimation of d dispersion; the s-d mixing is probably also too

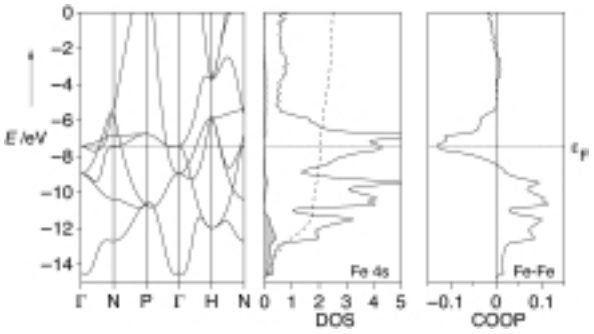

Figure 41. Band structure, DOS, and Fe-Fe COOP curves for nonmagnetic α-Fe calculated using the extended Hückel, tight-binding method.

strong. The chemically (or magnetically) most important finding is fully retained though: ε_F appears in a set of strongly Fe-Fe antibonding levels in each calculation, leading us to expect the presence of an instability with respect to ferromagnetism. Although it is impossible to carry out a spin-polarized calculation within this method itself, we believe that it can be used to rapidly screen metallic structures for a tendency to become ferromagnetic.

The parameters used in this extended Hückel, tight-binding calculation on α-Fe ($H_{ii}(4s) = -9.2$ eV, $\zeta(4s) = 1.9$, $H_{ii}(4p) = -3.8$ eV, $\zeta(4p) = 1.9$, $H_{ii}(3d) = -9.2$ eV, $\zeta_1(3d) = 5.35$, $\zeta_2(3d) = 1.80$, expansion coefficients $c_1(3d) = 0.5366$, $c_2(3d) = 0.6678$) were adapted from the standard metallic Fe parameter set[126] with modifications to the parameters for the 4s orbitals in order to reproduce the degree to which the 4s band penetrates the 3d block. The extended Hückel calculations were carried out using YAeHMOP.[127]

We would like to thank Prof. Heiko Lueken for useful and informative discussions, Wieland Wache for his assistance with some of the atomic and molecular calculations, Anne Gerber for help in preparing the final version of the manuscript, the Fonds der Chemischen Industrie for financial support, and Roald Hoffmann for the invaluable training he provided to both of the authors.

Received: 14. September 1999 [A 361]

[1] E. C. Stoner, *Rep. Prog. Phys.* **1946 – 1947**, *11*, 43.
[2] R. Hoffmann, *Acc. Chem. Res.* **1971**, *4*, 1.
[3] The actual number (104) was arrived at by counting the number of papers in *Phys. Rev. B* which contain words beginning with "ferromagnet" in the title. This is almost certainly an underestimate of the actual number of papers dealing with the topic.
[4] H. Lueken, *Magnetochemie – eine Einführung in Theorie und Anwendung*, Teubner, Stuttgart, **1999**.
[5] *Out of the Crystal Maze* (Eds.: L. Hoddeson, E. Braun, J. Teichmann, S. Weart), Oxford University Press, Oxford, **1992**.
[6] P. Curie, *Ann. Chim. Phys.* **1895**, *5*, 289.
[7] P. Langevin, *Ann. Chim. Phys.* **1905**, *5*, 70.
[8] P. Weiss, *J. Phys.* **1907**, *6*, 661.
[9] P. Weiss, *C. R. Acad. Sci. Paris* **1913**, *157*, 1405.
[10] W. Heisenberg, *Z. Phys.* **1928**, *49*, 619.
[11] P. A. M. Dirac, *Proc. R. Soc. London A* **1929**, *123*, 714.
[12] J. H. van Vleck, *The Theory of Electric and Magnetic Susceptibilities*, Oxford University Press, London, **1932**.
[13] Strong believers in the Heisenberg picture of ferromagnetism invoked the idea of "mixed valence" within elemental Fe, Co, and Ni in order to explain these moments. See, for example, refs. [128, 129]. This complicated mechanism, while effective, certainly does not satisfy Occam's razor. Also, the assumption of the presence of mixed-valence iron ions in metallic iron probably sounds bizarre (at best) to solid-state chemists.
[14] H. Krutter, *Phys. Rev.* **1935**, *48*, 664.
[15] J. C. Slater, *Phys. Rev.* **1936**, *49*, 537.
[16] E. C. Stoner, *Proc. R. Soc. London A* **1938**, *165*, 372.
[17] E. C. Stoner, *Proc. R. Soc. London A* **1939**, *169*, 339.
[18] O. K. Andersen, J. Madsen, U. K. Poulsen, O. Jepsen, J. Kollár, *Physica B* **1977**, *86 – 88*, 249.
[19] J. F. Janak, *Phys. Rev. B* **1977**, *16*, 255.
[20] C. Herring in *Magnetism*, *Vol. 4* (Eds.: G. Rado, H. Suhl), Academic Press, New York, **1966**.
[21] Within the spherical symmetry of the atomic calculation, the two polarization functions (with d and f symmetry) are not allowed to mix into these AOs.
[22] R. J. Boyd, *Nature* **1984**, *310*, 480.
[23] W. Kutzelnigg, *Angew. Chem.* **1984**, *96*, 262; *Angew. Chem. Int. Ed. Engl.* **1984**, *23*, 272.
[24] J. C. Slater, *Quantum Theory of Atomic Structure*, *Vol. I*, McGraw – Hill, New York, **1960**.
[25] We use the phrase "type of orbital" as a shorthand to distinguish orbitals with different angular-momentum quantum numbers, s, p, d, and so forth.
[26] E. Clementi, D. L. Raimondi, *J. Chem. Phys.* **1963**, *38*, 2686.
[27] G. Burns, *J. Chem. Phys.* **1964**, *41*, 1521.
[28] The technique of Clementi and Raimondi, with its focus on energy matching, effectively weights the regions of high electron density near the nucleus more heavily than those remote from the nucleus. However, these more distant regions play the primary role in chemical bonding.
[29] This quantity is not trivial to assign in the triplet calculations; we define it to be the splitting between the highest-occupied and the lowest-unoccupied α orbitals. We feel that this is the choice most analogous to that used in the singlet calculations.
[30] R. G. Pearson, *Chemical Hardness*, Wiley-VCH, Weinheim, **1997**.
[31] "Density-Functional Theory of Atoms and Molecules": R. G. Parr, W. Yang, *International Series of Monographs on Chemistry*, *Vol. 16*, Oxford University Press, New York, **1989**.
[32] B. Brecht, K. Weill, *Die Dreigroschenoper*, Universal-Edition, Vienna, **1928**.
[33] S. Chikazumi, *Physics of Ferromagnetism*, *2nd ed.*, Clarendon, Oxford, **1997**.
[34] We wish to once again emphasize that this electron-pairing energy is not solely a consequence of electron – electron repulsion. In fact, as we discussed above for atoms and molecules, the electron pairing associated with a transition from high spin to low spin actually *decreases* both the electron – electron repulsion and the electron – nuclear attraction energies. The electron – nuclear attraction is the term which is most responsible for the tendency of free atoms and molecules to adopt high-spin states.
[35] W. A. Harrison, *Electronic Structure and the Properties of Solids. The Physics of the Chemical Bond*, Dover, New York, **1989**.
[36] The results of inelastic neutron scattering experiments on α-Fe and other itinerant-electron ferromagnets indicate that the disappearance of ferromagnetism above T_c is not due to an absence of magnetic moments on each atom. The nonferromagnetic phases all exhibit strong short-range magnetic ordering; only the long-range ordering of these regions has been lost. It is as if the magnetic domains have become very small (on the order of tens of Ångströms) and disordered. This topic is discussed in depth in ref. [130], and references therein.
[37] H. Ibach, H. Lüth, *Solid-State Physics*, *2nd ed.*, Springer, Berlin, **1995**.
[38] There is a high-temperature bcc phase of Mn which is stable at around 1200 °C.[131] To the best of our knowledge, it has not been possible to quench this to a low temperature and measure its magnetic properties.
[39] S. C. Abrahams, L. Guttman, J. S. Kasper, *Phys. Rev.* **1962**, *127*, 2052.
[40] A. Onodera, Y. Tsunoda, N. Kunitomi, O. A. Pringle, R. M. Nicklow, R. M. Moon, *Phys. Rev. B* **1994**, *50*, 3532.
[41] An alternate approach for determining the chemical hardness of metals simply sets the hardness equal to the reciprocal of the density

of states at the Fermi level,[132] requiring the implicit assumption that the slope of DOS(E) at ε_F is equal to zero. This is clearly not the case for many of the elemental transition metals (see Figure 21).
[42] J. Hubbard, *Proc. R. Soc. London A* **1963**, *276*, 238.
[43] For a qualitative overview of the Hubbard model see, for example, chapter 5 of ref. [133].
[44] *Electron Correlation and Magnetism in Narrow-Band Systems* (Ed.: T. Moriya), Springer, Berlin, **1981**.
[45] H. Tasaki, *Prog. Theor. Phys.* **1998**, *99*, 489.
[46] R. Strack, D. Vollhardt, *Phys. Rev. Lett.* **1994**, *72*, 3425.
[47] M. Kollar, R. Strack, D. Vollhardt, *Phys. Rev. B* **1996**, *53*, 9225.
[48] J. E. Hirsch, *Phys. Rev. B* **1989**, *40*, 2354.
[49] J. E. Hirsch, *Phys. Rev. B* **1989**, *40*, 9061.
[50] J. E. Hirsch, *Phys. Rev. B* **1990**, *67*, 4549.
[51] S. Tang, J. E. Hirsch, *Phys. Rev. B* **1990**, *42*, 771.
[52] J. E. Hirsch, *Phys. Rev. B* **1991**, *43*, 705.
[53] J. C. Amadon, J. E. Hirsch, *Phys. Rev. B* **1996**, *54*, 6364.
[54] J. E. Hirsch, *Phys. Rev. B* **1997**, *56*, 11022.
[55] D. Vollhardt, N. Blümer, K. Held, M. Kollar, J. Schlipf, M. Ulmke, J. Wahle, *Adv. Solid State Phys.* **1999**, *38*, 383.
[56] L. H. Thomas, *Proc. Cambridge Philos. Soc.* **1927**, *23*, 542.
[57] E. Fermi, *Atti. Accad. Naz. Lincei Cl. Sci. Fis. Mat. Nat. Rend.* **1927**, *6*, 602.
[58] E. Fermi, *Z. Phys.* **1928**, *48*, 73.
[59] E. Fermi, *Atti. Accad. Naz. Lincei Cl. Sci. Fis. Mat. Nat. Rend.* **1928**, *7*, 342.
[60] P. Hohenberg, W. Kohn, *Phys. Rev. B* **1964**, *136*, 864.
[61] W. Kohn, L. J. Sham, *Phys. Rev. A* **1965**, *140*, 1133.
[62] J. C. Slater, *Phys. Rev.* **1951**, *81*, 385.
[63] U. von Barth, L. Hedin, *J. Phys. C* **1972**, *5*, 1629.
[64] L. Fritsche, B. Weimert, *Phys. Status Solidi B* **1998**, *208*, 287.
[65] S. H. Vosko, J. P. Perdew, *Can. J. Phys.* **1975**, *53*, 1385.
[66] O. Gunnarsson, *J. Phys. F* **1976**, *6*, 587.
[67] V. L. Moruzzi, J. F. Janak, A. R. Williams, *Calculated Electronic Properties of Metals*, Pergamon, New York, **1978**.
[68] J. Kübler, *Phys. Lett. A* **1981**, *81*, 81.
[69] C. S. Wang, B. M. Klein, H. Krakauer, *Phys. Rev. Lett.* **1985**, *54*, 1852.
[70] P. Bagno, O. Jepsen, O. Gunnarsson, *Phys. Rev. B* **1989**, *40*, 1997.
[71] V. L. Moruzzi, P. M. Marcus, K. Schwarz, P. Mohn, *Phys. Rev. B* **1986**, *34*, 1784.
[72] V. L. Moruzzi, P. M. Marcus, *Phys. Rev. B* **1988**, *38*, 1613.
[73] V. L. Moruzzi, P. M. Marcus, *Phys. Rev. B* **1989**, *39*, 471.
[74] V. L. Moruzzi, P. M. Marcus, *Phys. Rev. B* **1990**, *42*, 8361.
[75] V. L. Moruzzi, P. M. Marcus, *Phys. Rev. B* **1990**, *42*, 10322.
[76] A. Simon, *Angew. Chem.* **1983**, *95*, 94; *Angew. Chem. Int. Ed. Engl.* **1983**, *22*, 95.
[77] P. Villars, L. D. Calvert, *Pearson's Handbook of Crystallographic Data for Intermetallic Phases, 2nd ed.*, ASM International, Ohio, **1991**.
[78] R. Smoluchowski, *J. Phys. Radium* **1951**, *12*, 389.
[79] While net charges derived from LMTO-ASA calculations are notoriously unreliable due to the fact that they scale with the sizes of the atomic spheres, here we compare two systems with identical sets of spheres. Consequently, the differences seen in calculated charges reflect the actual charge redistribution fairly well.
[80] K. H. J. Buschow, P. G. van Engen, R. Jongebreur, *J. Magn. Magn. Mater.* **1983**, *38*, 1.
[81] J. Jääskeläinen, E. Suoninen, *Phys. Status Solidi A* **1981**, *63*, 241.
[82] Y. V. Palguyev, A. A. Kuranov, P. N. Syutkin, F. A. Didorenko, *Phys. Met. Metallogr. (Engl. Transl.)* **1976**, *42*, 46.
[83] E. F. Wassermann in *Ferromagnetic Materials*, *Vol. 5* (Eds.: K. H. J. Buschow, E. P. Wohlfarth), North Holland, Amsterdam, **1990**, p. 250.
[84] S. K. Bose, J. Kudrnovsky, M. van Schilfgaarde, P. Blöchl, O. Jepsen, M. Methfessel, A. T. Paxton, O. K. Andersen, *J. Magn. Magn. Mater.* **1990**, *87*, 97.
[85] P. Mohn, E. Supanetz, K. Schwarz, *Aust. J. Phys.* **1993**, *46*, 651. This paper includes energy surface calculations for all three alloys, assuming perfectly ordered crystal structures.
[86] J. W. Cable, W. O. Wollan, W. C. Koehler, *J. Appl. Phys.* **1963**, *34*, 1189.
[87] G. P. Felcher, J. W. Cable, M. K. Wilkinson, *J. Phys. Chem. Solids* **1963**, *24*, 1663.
[88] U. Müller, *Anorganische Strukturchemie*, Teubner, Stuttgart, **1992**.
[89] W. J. Takei, D. E. Coc, G. Shirane, *Phys. Rev.* **1963**, *129*, 2008.
[90] H. Nagasaki, I. Wakabayashi, S. Minomura, *J. Phys. Chem. Solids* **1969**, *30*, 329.
[91] W. Reimers, E. Hellner, W. Treutmann, P. J. Brown, *J. Phys. Chem. Solids* **1983**, *44*, 195.
[92] R. Dronskowski, P. E. Blöchl, *J. Phys. Chem.* **1993**, *97*, 8617.
[93] M. A. Rudermann, C. Kittel, *Phys. Rev.* **1954**, *96*, 99.
[94] T. Kasuya, *Prog. Theor. Phys.* **1956**, *16*, 45.
[95] K. Yosida, *Phys. Rev.* **1957**, *106*, 893.
[96] P. Soven, *Phys. Rev.* **1967**, *156*, 809.
[97] J. L. Beeby, *Proc. R. Soc. London A* **1967**, *302*, 113.
[98] P. Soven, *Phys. Rev.* **1969**, *178*, 1136.
[99] J. S. Faulkner, *Prog. Mater. Sci.* **1982**, *27*, 1.
[100] A. Decker, G. A. Landrum, R. Dronskowski, unpublished results.
[101] M.-H. Whangbo, R. Hoffmann, *J. Am. Chem. Soc.* **1978**, *100*, 6093.
[102] M.-H. Whangbo, R. Hoffmann, R. B. Woodward, *Proc. R. Soc. London A* **1979**, *366*, 23.
[103] N. W. Ashcroft, N. D. Mermin, *Solid State Physics*, Saunders College Publishing, New York, **1976**.
[104] O. K. Andersen, *Phys. Rev. B* **1975**, *12*, 3060.
[105] H. L. Skriver, *The LMTO Method*, Springer, Berlin, **1984**.
[106] O. K. Andersen in *The Electronic Structure of Complex Systems* (Eds.: P. Phariseau, W. M. Temmerman), Plenum, New York, **1984**.
[107] "Tight-Binding Approach to Computational Materials Science": O. K. Andersen, C. Arcangeli, R. W. Tank, T. Saha-Dasgupta, G. Krier, O. Jepsen, I. Dasgupta, *Mater. Res. Soc. Symp. Proc.* **1998**, *491*, 3.
[108] P. E. Blöchl, O. Jepsen, O. K. Andersen, *Phys. Rev. B* **1994**, *49*, 16223.
[109] G. Krier, O. Jepsen, A. Burkhardt, O. K. Andersen, The TB-LMTO-ASA Program, Version 4.7.
[110] LAPW calculations were carried out using the program WIEN97,[111] which is an improved and updated Unix version of the original copyrighted WIEN[134].
[111] P. Blaha, K. Schwarz, J. Luitz, Vienna University of Technology, **1997**, program WIEN97.
[112] R. Hoffmann, *Solids and Surfaces: A Chemist's View of Bonding in Extended Structures*, VCH, Weinheim, **1988**.
[113] T. Hughbanks, R. Hoffmann, *J. Am. Chem. Soc.* **1983**, *105*, 3528.
[114] E. J. Baerends, D. E. Ellis, P. Ros, *Chem. Phys.* **1973**, *2*, 41.
[115] G. te Velde, E. J. Baerends, *J. Comp. Phys.* **1992**, *99*, 84.
[116] C. Fonsecca Guerra, O. Visser, J. G. Snijders, G. te Velde, E. J. Baerends in *Methods and Techniques for Computational Chemistry* (Eds.: E. Clementi, C. Corongiu), STEF, Cagliari, **1995**, p. 305.
[117] J. G. Snijders, E. J. Baerends, P. Vernoojis, *At. Nucl. Data Tables* **1982**, *26*, 483.
[118] S. H. Vosko, L. Wilk, M. Nusair, *Can. J. Phys.* **1980**, *58*, 1200.
[119] A. D. Becke, *Phys. Rev. A* **1988**, *38*, 3098.
[120] C. Lee, W. Yang, R. G. Parr, *Phys. Rev. B* **1988**, *37*, 785.
[121] G. A. Landrum, Viewkel version 3.0, **1999**, is freely available on the WWW at http://overlap.chem.cornell.edu:8080/yaehmop.html.
[122] R. Hoffmann, *J. Chem. Phys.* **1963**, *39*, 1397.
[123] R. Hoffmann, *J. Chem. Phys.* **1964**, *40*, 2745.
[124] R. Hoffmann, *J. Chem. Phys.* **1964**, *40*, 2474.
[125] *"Extended Hückel is the theory to which all others are superior."* Roald Hoffmann.
[126] S. Alvarez, Barcelona (Spain), unpublished tabulation, **1993**.
[127] G. A. Landrum, W. V. Glassey, YAeHMOP, **1999**, is freely available on the WWW at http://overlap.chem.cornell.edu:8080/yaehmop.html.
[128] J. H. van Vleck, *Rev. Mod. Phys.* **1945**, *17*, 27.
[129] J. H. van Vleck, *Physica* **1949**, *15*, 197.
[130] H. Capellmann, *J. Magn. Magn. Mater.* **1982**, *28*, 250.
[131] Z. S. Basinski, J. W. Christian, *Proc. R. Soc. London A* **1954**, *223*, 554.
[132] W. Yang, R. G. Parr, *Proc. Natl. Acad. Sci. USA* **1985**, *82*, 6723.
[133] A. Cox, *The Electronic Structure and Chemistry of Solids*, Oxford University Press, Oxford, **1987**.
[134] P. Blaha, K. Schwarz, P. Sorantin, S. B. Trickey, *Comput. Phys. Commun.* **1990**, *59*, 399.